Atmospheric Research 340 (2026) 109016

Contents lists available at ScienceDirect

Atmospheric Research

journal homepage: www.elsevier.com/locate/atmosres

Impacts of the future Amazon deforestation on the precipitation over the Peruvian central Andes and related atmospheric features

Miguel Saavedra [a,b,*], Clementine Junquas [c,d], Ken Takahashi [a], Yamina Silva [a,b], Jhan-Carlo Espinoza [c,e], Juan-Pablo Sierra [f]

[a] Dirección de Ciencias de la Atmósfera e Hidrósfera y Cambio Climático, Instituto Geofísico del Perú, Lima 15012, Peru
[b] Pontificia Universidad Católica del Perú (PUCP), Lima, Peru
[c] University Grenoble Alpes, IRD, CNRS, Grenoble INP, IGE, Grenoble, France
[d] Servicio Nacional de Meteorología e Hidrología (SENAMHI), Lima 15072, Peru
[e] Instituto de Investigación sobre la Enseñanza de las Matemáticas, Pontificia Universidad Católica del Perú (PUCP), Lima, Peru
[f] Laboratoire de Météorologie Dynamique (LMD), IPSL, CNRS, École Polytechnique, Palaiseau, Paris, France

ARTICLE INFO

Keywords:
Amazon deforestation
Andes precipitation
WRF model
Mantaro Basin

ABSTRACT

This study investigates the impact of a 40% Amazon deforestation scenario (projected for 2050) on precipitation over the central Peruvian Andes during five austral summer seasons (DJF 2001–2006) using high-resolution (1 km) WRF simulations. While a widespread rainfall reduction pattern is observed over the Amazon-Andes transition zone, statistically significant decreases ($p < 0.10$) at the gridpoint level are primarily concentrated near rainfall hotspots in the Amazon-Andes transitions zone, reaching an average reduction of 12% (-1.4 mm day^{-1}). This drying signal is physically associated with a weakening of the South American Low-Level Jet (LLJ) and reduced moisture influx, which specifically inhibits convective activity during the morning peak hours (23–11 LT). In the high-altitude Mantaro Basin, we observe a consistent drying pattern (-5%) that extends from the transition zone; although these changes are not statistically significant due to high interannual variability, the physical signal of precipitation reduction and dry air advection remains clear. Conversely, the western Andean ridges exhibit a localized precipitation increase (up to 20%) linked to intensified cross-barrier easterly wind anomalies reinforcing diurnal anabatic circulation. We further find that while 5 km resolution captures broad basin-scale patterns, convection-permitting scales (1 km) are essential for resolving these complex topographic effects. These findings highlight a critical vulnerability concentrated along the eastern slopes and the high Andes. The identified drying patterns, which are particularly pronounced in the Andes-Amazon transition zone (a global biodiversity hotspot) and extend into the highlands, pose a significant threat to endemic ecosystems and regional water security, specifically through reservoir inflow reduction and negative impacts on agriculture.

1. Introduction

The central region of Peru is characterized by a stark geographical transition, with the Andes mountains separating the arid coast from the humid Amazon Basin. This region is of critical national importance, hosting a significant portion of the country's population; the departments of Lima and Junín alone concentrate 32% and 4% of the national total, respectively. This region has extensive agricultural land (2.0 million hectares in Lima and 2.4 million in Junín) that, besides supplying food for domestic consumption, also produces key export crops like coastal sugarcane and coffee from the Andes-Amazon transition zone. At the heart of this region lies the Mantaro Basin, a vital hub for both food and energy. As a primary agricultural valley, it supplies staple foods to major urban centers like Lima, while its hydroelectric complex generates a substantial 19% of Peru's national electricity. (INEI, 2021a, 2021b; Instituto Geofísico del Perú, 2005). The region is also distinguished by its remarkable biodiversity. This natural wealth is largely concentrated in the Andes-Amazon transition zone, an area recognized as a global hotspot due to its high concentration of endemic species and unique ecosystems driven by steep environmental gradients (MINAM, 2012; e.g. Mittermeier et al., 2011; Asner et al., 2017). Despite this profound socioeconomic and ecological importance,

* Corresponding author at: Dirección de Ciencias de la Atmósfera e Hidrósfera y Cambio Climático, Instituto Geofísico del Perú, Lima 15012, Peru.
E-mail address: msaavedra@igp.gob.pe (M. Saavedra).

https://doi.org/10.1016/j.atmosres.2026.109016
Received 21 May 2025; Received in revised form 13 April 2026; Accepted 14 April 2026
Available online 15 April 2026

its associated climate processes are still little studied.

Precipitation over central Peru, including the coastal, Andean, and Amazon regions, follows a unimodal regime with a maximum close to the austral summer months (Espinoza Villar et al., 2009; Lavado Casimiro et al., 2013; Segura et al., 2019). This region is characterized by an exceptional rainfall gradient, from almost zero mm/year on the central Peruvian coast to more than 6000 mm/year on the eastern flank of the Andes (Espinoza et al., 2015; Rau et al., 2017; Chavez and Takahashi, 2017). In addition, the seasonal range tends to be high over the Andes Mountains with more than 50% of the annual occurring during austral summer (e.g. Saavedra and Takahashi, 2017; Espinoza et al., 2020; Giráldez et al., 2020). Other studies have shown that an increase in precipitation over Peru is associated with easterly anomalies at higher levels, closely related to the Bolivian High, and also with the moisture advection from the Amazon lowlands driven by the northerly flux associated with the LLJ along the eastern face of the Andes (e.g., Garreaud, 2009; Sulca et al., 2016; Chavez and Takahashi, 2017; Junquas et al., 2018; Kumar et al., 2019; Segura et al., 2020; Klein et al., 2023).

The Amazon, due to its great forest resources, is one of the most important sources of atmospheric moisture, where 25–35% of the precipitation is returned to the atmosphere as water vapor to form precipitation (Benton et al., 1950; Eltahir and Bras, 1994; Burde et al., 2006). Furthermore, evapotranspiration from the Amazon Basin contributes over 30% to the annual precipitation over the central Andes of Peru (e.g. Staal et al., 2018; Dirmeyer et al., 2009), thus highlighting the importance of processes that involve water dynamics between the Amazon and the Andes. However, some continental-scale modeling studies have shown that this moisture recycling could be modified by the effects of deforestation, such as the conversion from forest to pasture, leading to a reduction in evapotranspiration (e.g., Costa and Foley, 2000; Sampaio et al., 2007; Swann et al., 2015). This mechanism is central to understanding the Amazon River basin, which is currently considered a biophysical system in transition (Davidson et al., 2012; Nobre et al., 2016). An increase in deforestation (Debortoli et al., 2017; Leite-Filho et al., 2021) is a main driver of this transition, in combination with a lengthening of the dry season in Southern Amazonia (Fu et al., 2013; Espinoza et al., 2021) and an increase in extreme droughts (Espinoza et al., 2024). Due to these environmental changes, a possible tipping point is being discussed within the scientific community, which would lead the Amazon rainforest to a new state with conditions similar to those of a savanna (Nobre and Borma, 2009; Hirota et al., 2011; Wongchuig et al., 2022). Amazon deforestation, mainly driven by agricultural and pasture expansion (Swann et al., 2015; Malhi et al., 2008), has been occurring for a long time, and the highest rate was reached around 2005, with values near 25 km^2yr^{-1} (Silva Junior et al., 2021). Then it decreased relatively fast until 2012 (below 5000 km^2yr^{-1}) but has subsequently increased more slowly up to the current date (11,000 km^2yr^{-1}), indicating that deforestation in the Amazon, while fluctuating, continues. In that respect and following a deforestation rate from 1997 to 2002 in a business-as-usual scenario, Soares-Filho et al. (2006) estimate that the Amazon deforestation could reach 40% of the basin by 2050. Studies on various deforestation scenarios have consistently found that reduced evapotranspiration is associated with an increase in albedo, decrease in leaf area, root depth, and surface roughness of the land cover such as the conversion from forest to grassland or cropland (Eltahir and Bras, 1994; Costa and Foley, 2000; Sampaio et al., 2007; Costa et al., 2007).

Furthermore, numerical modeling has been an essential part of the study in the Andes region, particularly those developed at high spatio-temporal resolution with the WRF model. Some studies based on regional models have shown a good representation of the rainfall diurnal cycle over the complex topography. For example, Saavedra et al. (2020) indicate that the precipitation peak on the western Andes is well simulated during the afternoon, which is consistent with observations and suggests a good representation of anabatic winds generated by daytime surface heating. In addition, as also found by Mourre et al. (2016), model representation of precipitation peaks over the embedded basins of the Andes is reached during the late afternoon or after the sunset, consistent with sub-daily observed data. These authors also refer to an overestimation of precipitation over basins and over the eastern slope of the Andes. Over the western slope of the Andes, Saavedra et al. (2020) show underestimation of precipitation. Other studies have also found that the diurnal cycle in the Andes can be well represented by high-resolution models, although with biases in the daily accumulated precipitation (e.g., Junquas et al., 2018, 2022; Rosales et al., 2022).

In this context, a recent modeling experiment by Sierra et al. (2022) provided a crucial baseline. Using the 40% Amazon deforestation scenario (Soares-Filho et al., 2006), they found that precipitation over the eastern Andean hillside in Bolivia could be reduced by up to 30%. This change was associated with a less intense LLJ under the deforested scenario.

However, this foundational study, which focused on the Bolivian Andes left two critical scientific gaps: First, it remains unknown how these deforestation impacts propagate further inland across the topography of the central Peruvian Andes to affect vital, high-altitude inter-Andean basins, such as the Mantaro Basin. Second, their work did not assess whether 5 km resolution is sufficient, or if convection-permitting scales (e.g., 1 km) are necessary to accurately capture impacts from the Andes-Amazon transition to the highlands of the Central Peruvian Andes.

Therefore, this research provides a novel contribution by explicitly addressing these gaps. We aim to: (1) Quantify precipitation changes across the full Amazon-Andes gradient (10°S - 14°S), from the Andes-Amazon transition zone to the high-altitude Mantaro Basin. (2) Diagnose the specific atmospheric mechanisms (e.g., LLJ weakening, moisture advection) that govern the inland propagation or buffering of the deforestation signal. (3) Evaluate the scale-dependence of these processes by comparing our 1 km results with simulations at 5 km resolution.

The next section (Section 2) explains the WRF model configuration and data used. Section 3 presents the simulation results, followed by a discussion (Section 4) and conclusions (Section 5).

2. Data and methods

2.1. Model description and experimental design

We performed experiments using the WRF model, which was designed for operational and research applications (Skamarock et al., 2019). Due to the complex topography of the study zone, a high spatio-temporal (1 km–1 h) resolution with 49 vertical levels was used. This model has been widely used in mountainous regions worldwide, including the Andes (e.g. Mourre et al., 2016; Junquas et al., 2018; Moya-Alvarez et al., 2018; Trachte et al., 2018). The main area covered, physics parameterization schemes and experimental design are summarized in Table 1. The chosen physics is consistent with those used by Sierra et al. (2022) and the cumulus scheme was deactivated, which is appropriate for convection-permitting scales.

Over the study zone, we consider two experiments at very high spatio-temporal resolution (D03, 1 km) which are forced by data obtained previously by Sierra et al. (2022). These experiments, which represent non-deforested and deforested conditions, are called CTL and DEF, respectively.

The forcing data from Sierra et al. (2022) were generated using a one-way nesting approach. First, a coarse domain (D01) at 15 km resolution was forced using ERA5 reanalysis data (Hersbach et al., 2020). Subsequently, the output from D01 was used to force a nested domain (D02) at 5 km resolution. This process was conducted for two different Amazon land-use scenarios: (i) the non-deforested CTL run, based on 2002 Amazon conditions according to Eva et al. (2004) (Fig. 1a); and (ii) the 40% deforestation DEF run, based on a business-as-usual scenario (Soares-Filho et al., 2006; Fig. 1b) applied to the non-deforested one.

Table 1
Summary of WRF Model Configuration and Experimental Design.

	D01 (Forcing - Sierra et al., 2022)	D02 (Forcing - Sierra et al., 2022)	D03 (This Study)
Spatial resolution	15 km	5 km	1 km
Main area covered	Northern South America	From central Peru to Bolivia	Central Peruvian Andes
Forcing Data	ERA5 (Hersbach et al., 2020)	One-way output from D01	One-way output from D02
Model schemes	Microphysics: Purdue and Lin (Chen and Sun, 2002) Boundary Layer (PBL): Yonsei University (Hong et al., 2006) Surface Layer: MM5 similarity (Paulson, 1970) Radiation (Longwave): RRTM (Mlawer et al., 1997) Radiation (Shortwave): Dudhia (Dudhia, 1989) Cumulus: Grell 3D (Grell and Dévényi, 2002) → Deactivated for D03		
CTL Land-Use	From Eva et al. (2004) (non-deforested)		
DEF Land-Use	As in CTL + deforestation according to Soares-Filho et al. (2006)		As in CTL

Specifically, the deforestation scenario implies the replacement of the Evergreen Broadleaf Forest (USGS 24-category class 13) with the Cropland/Grassland Mosaic category (USGS 24-category class 5). This land-use modification drastically alters surface properties, primarily reducing the roughness length (approx. From 0.50 m to 0.10 m), Leaf Area Index (approx. From 5.5 to 3.5 m^2 m^{-2}), and vegetation fraction (approx. From 0.95 to 0.80), while increasing surface albedo (approx. From 0.12 to 0.20). Land-use data is at 1 km spatial resolution. Further details about simulations in D01 and D02 can be found in Sierra et al. (2022).

Finally, the results from the D02 domain (for both CTL and DEF runs) were employed to force our experiments within D03. It is important to note that no land-use change was applied within the high-resolution domain (D03), so the land-use remained identical in both the CTL and DEF experiments (using the non-deforested land cover from Eva et al. (2004), see Fig. 1c). Therefore, the study zone in D03 is impacted only by the differing lateral boundary conditions provided by the D02 simulations. Simulations were performed for five austral summer seasons, from 2001–2002 to 2005–2006. The selection of these five periods was constrained by the significant computational expense of 1-km resolution simulations and the availability of forcing data from Sierra et al. (2022). However, this period provides a valuable opportunity to assess the deforestation impact under diverse large-scale climatic conditions. Based on the Niño 3.4 index (Fig. S1), this 5-year window captures a robust range of interannual variability. It includes a moderate El Niño (2002−2003), a weak El Niño (2004–2005), a moderate La Niña (2005–2006), and two ENSO-neutral seasons (2001–2002, 2003–2004). This diversity allows us to analyze the robustness of the deforestation signal across a representative set of large-scale climate states. For each season, the simulations were initialized on November 26 and run continuously through February 27. The first 14 days of each simulation (November 26 – December 9) were discarded as the spin-up period. This extended period was chosen to ensure the model's soil moisture fields and the convective regimes reached a stable equilibrium before the start of the analysis period on December 10. Consequently, the effective analysis covers 80 days per wet season (from December 10 to February 27), resulting in a total sample size of 400 days.

2.2. In-situ and gridded data

To validate the CTL simulation, we utilized rainfall in-situ data collected from 55 meteorological stations managed by the Servicio Nacional de Meteorología e Hidrología del Perú (SENAMHI) (Table S1). The stations are distributed as follows: 30 along the western slope of the Andes, 21 in the Mantaro Basin and 4 on the eastern slope. All these stations were selected based on their low percentage of data gaps, with less than 10% of missing data. Specifically, out of the 55 selected stations, 34 have a complete daily record, and 51 have at least 95% data availability. Because most of the network (> 90%) has nearly complete records, no temporal gap-filling techniques were applied to avoid introducing artificial interpolation errors over the complex topography. The dataset includes daily information from December to February for the years 2001–2002 through 2005–2006.

To compare with precipitation data, the Peruvian Interpolated data of SENAMHI's Climatological and Hydrological Observations (PISCO) dataset with a spatial resolution of 0.05° and a temporal resolution of one day was used. PISCO is a database established by SENAMHI and covers the entire Peruvian territory (Aybar et al., 2020). Compared to other similar products, such as CHIRPS (Funk et al., 2015), PISCO incorporates a more extensive range of in-situ precipitation stations, providing a more comprehensive picture of precipitation patterns across the country. However, it is important to acknowledge the inherent uncertainties of this observational benchmark over complex topography. Although PISCO merges these in-situ observations with satellite-based climatological datasets, its accuracy remains constrained by the heterogeneous spatial density of the underlying station network. Consequently, in sparsely monitored high-elevation areas and the Amazon transition, the product can introduce localized uncertainties (Aybar et al., 2020). Despite these limitations, PISCO and the in-situ network serve as our primary benchmarks to evaluate the CTL simulation. This quantitative assessment, based on absolute bias, relative bias, and Pearson correlation, is detailed in Section 3.1.

For a more focused analysis, some subregions (boxes) have been defined within the study zone: the highlands of the western slope of the Andes (WSA), the Central Mantaro Basin (CMB), the Southern Mantaro Basin (SMB) and the Amazon-Andes transition (AMA) (Fig. 2a). These subregions cover distinct topographic ranges: WSA (2200–5200 m a.s.l.), CMB (3200–4400 m a.s.l.), SMB (1600–4500 m a.s.l.), and AMA (300–1800 m a.s.l.). The number of in-situ data points within these subregions is six, five, seven, and one, respectively. These four locations are utilized to validate the year-to-year behavior of CTL and to make comparisons between CTL and DEF conditions. In addition, a precipitation hotspot zone is taken into account inside the AMA subregion.

To contrast the diurnal cycle of simulations over these subregions with more realistic data, we use a precipitation product (hereafter called P2A25) obtained from the TRMM's Precipitation Radar (TRMM-PR, version 7, product 2A25). P2A25 was obtained from a series of swaths to calculate an average value from November(0) to February (1) months between 1998 and 2012, averaged every three hours with a 5 km spatial resolution. This product was previously used by Junquas et al. (2018) to compare with WRF outputs at 9 km spatial resolution, encountering lower values than the model. More details about P2A25 can be found in Chavez and Takahashi (2017).

Finally, the NOAA Optimum Interpolation Sea Surface Temperature Version 2 (Reynolds et al., 2002) was utilized to obtain sea surface temperature (SST) indices, which may be associated with interannual variability of the modeled precipitation. We compute anomalies of three-month running means for the Niño 3.4 (5°S-5°N, 170°W-120°W), the Niño 1+2 (10°S-0°N, 90°W-80°W) and Tropical North Atlantic (TNA) (5°N-25°N, 55°W-15°W) regions. The climatology for these computations was based on the period 1981–2010.

2.3. Changes and statistical significance

To quantify the changes induced by deforestation (DEF relative to CTL), we analyzed daily values derived from the hourly simulation outputs. For continuous variables (such as wind components, specific humidity, and moisture flux) daily values were computed as the 24-h mean. In contrast, daily precipitation was calculated as the 24-h accumulation. Additionally, to analyze changes in the diurnal cycle, we constructed specific time series for each hour of the day across the entire

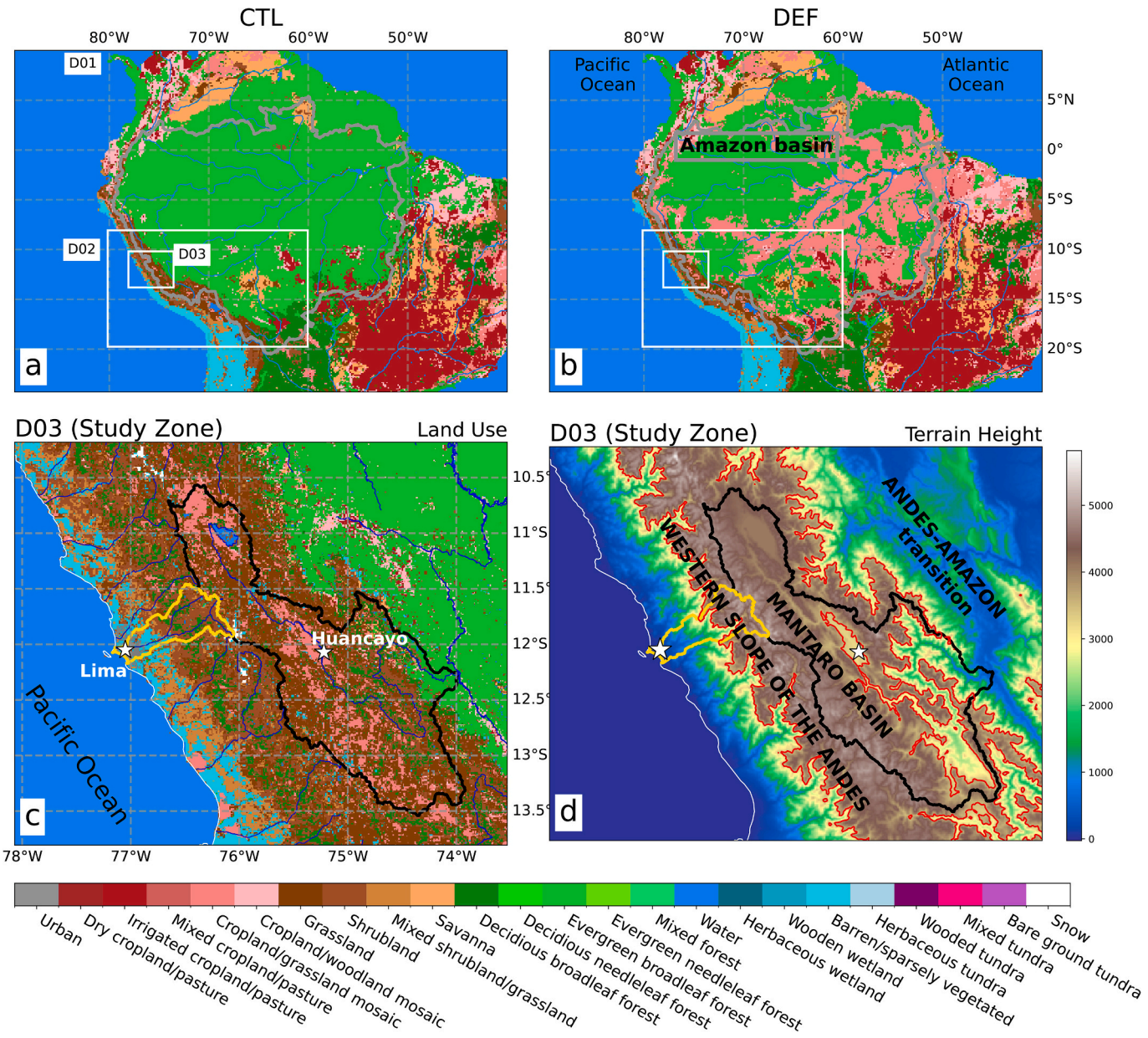

Fig. 1. WRF domain configuration and land-use scenarios. (a) Land use for the D01 (15 km) and D02 (5 km) domains in the CTL (non-deforested) simulation. (b) Land use for the D01 and D02 domains in the DEF (40% deforestation) simulation. The box for D03 in (a) and (b) indicates the location of the D03 domain, which is shown in detail in (c). The Amazon Basin is delimited by the thick gray line. (c) High-resolution (1 km) land use for the D03 domain (Study Zone). This specific land-use map was used for both the CTL and DEF simulations. The Mantaro (black) and Rimac (yellow) basins are outlined. (d) Orography (terrain height) for the D03 domain, showing key regions. (For interpretation of the references to colour in this figure legend, the reader is referred to the web version of this article.)

400-day period.

To assess the statistical significance of the differences between the experiments, we applied the Circular Block Bootstrapping (CBB) method. As described by Wilks (2019), this non-parametric approach is specifically suitable for daily meteorological data because it preserves the inherent serial correlation of the time series by resampling blocks of consecutive data rather than individual time steps.

The analysis was performed on the total sample of $n = 400$ time steps. A distinctive feature of our approach is that the optimal block length, L, was determined locally for each individual grid point, irrespective of the domain geometry of the analysis. That is, an independent L was calculated for each series corresponding to any point in horizontal space, vertical cross-sections, or time-height profiles. To compute L, we solved the implicit optimization function recommended by Wilks (2019):

$$L = (n - L + 1)^{\frac{2}{3}\left(1-\frac{n'}{n}\right)}$$

Where n' represents the local effective sample size based on the lag-1 autocorrelation coefficient. Furthermore, the significance test was performed treating the CTL and DEF distributions as unpaired (independent) samples. This approach yields a conservative estimate of significance by not removing the shared internal variability (covariance) between the simulations, thereby ensuring that the detected signals represent robust deviations that exceed the larger variance estimate of the unpaired test. However, it is important to note that these significance tests were performed independently for each grid point (i.e., on a gridpoint-by-gridpoint basis) without applying any spatial multiplicity correction. Consequently, the spatially distributed significance markers in our figures represent local significance and should be interpreted with

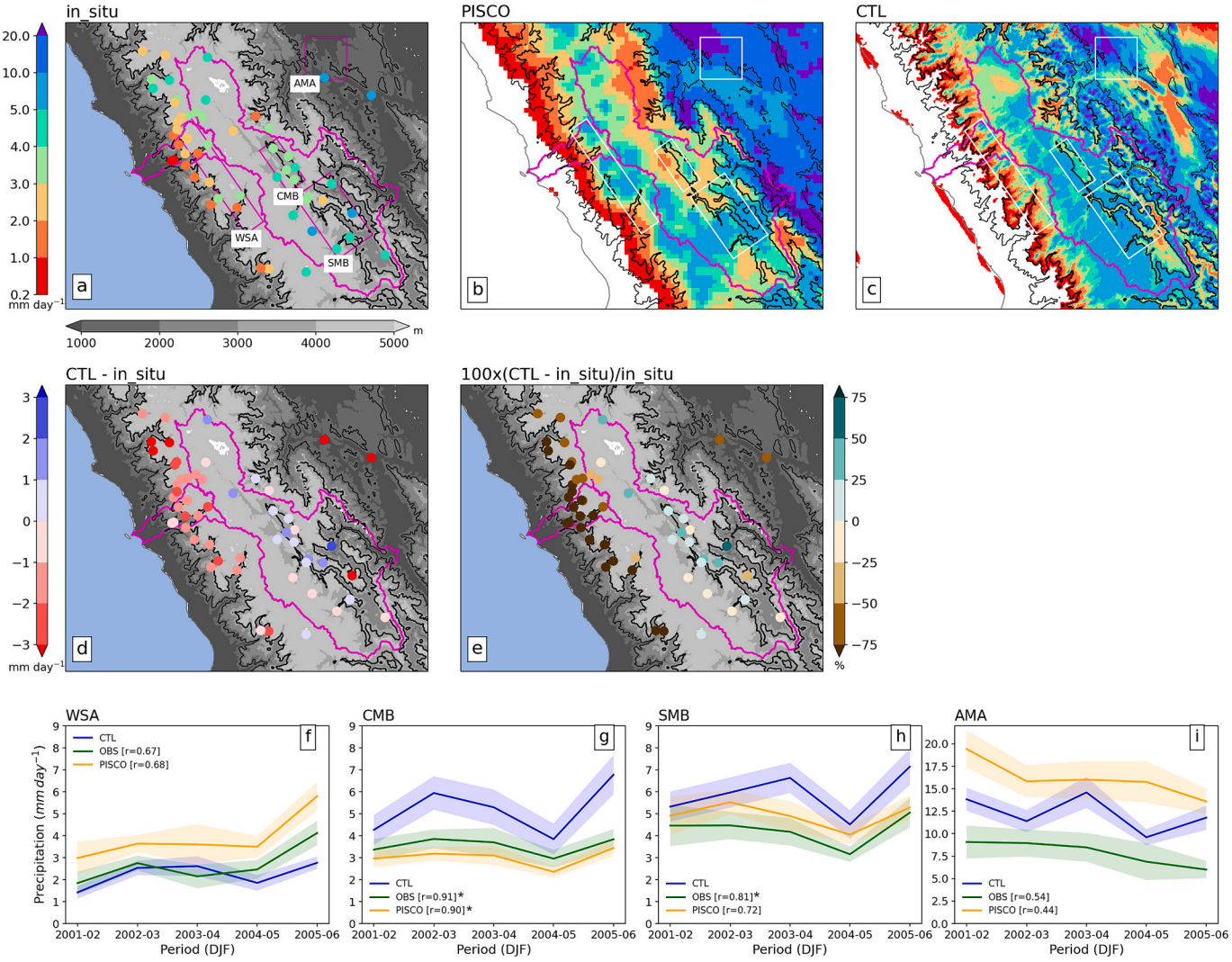

Fig. 2. (a) Average in-situ precipitation for 55 SENAMHI stations over the study area. (b) Precipitation from the PISCO database. (c) Average precipitation for the CTL simulation. (d) Precipitation bias and (e) relative precipitation bias. The Mantaro and Rimac Basins are delimited by magenta lines. Black contour lines indicate the 1500 and 3500 m a.s.l. levels. Panels (f–i) show the interannual variability of wet-season precipitation for CTL, in-situ data (OBS), and PISCO in the WSA, CMB, SMB, and AMA subregions, respectively. Shaded areas indicate the standard error, and r denotes the Pearson's correlation coefficients between the reference datasets (OBS and PISCO) and CTL. An asterisk (*) indicates statistical significance at p-value <0.10. (For interpretation of the references to colour in this figure legend, the reader is referred to the web version of this article.)

this limitation in mind.

Finally, the CBB method was also utilized to estimate the standard error of the seasonal mean precipitation for the analyzed subregions (WSA, CMB, SMB, and AMA). In this specific application, the bootstrapping was performed on the average daily time series ($n = 80$ days) for each wet season independently, ensuring that the serial correlation of the regional averages was properly accounted for.

3. Results

3.1. Validation of rainfall patterns

Fig. 2a shows the mean in situ precipitation over the study zone. We encountered low values on the western slope of the Andes, with a maximum of 4 mm day^{-1} over the highest parts and a minimum of 1.0 mm day^{-1}. We found higher values over the Mantaro Basin, where most of them range from 3.0 to 5.0 mm day^{-1}. In the lowland valleys of the eastern side of the Andes, values can reach 8 mm day^{-1}, while lower values can be detected in the two sites located in the highlands, next to the Mantaro Basin. These in situ data values are consistent with previous works (e. g. Lavado Casimiro et al., 2013; Giráldez et al., 2020, Trachte et al., 2018). Overall, we observe an increasing precipitation gradient in the northeastward direction, a pattern that is also well depicted by the PISCO dataset (Fig. 2b).

Average daily precipitation from the CTL experiment for all periods is shown in Fig. 2c. Similar to the gridded PISCO dataset, higher precipitation values are observed toward the northeast. Locally, over the western Andes, both CTL and PISCO indicate higher precipitation along the ridges and lower values in the valley bottoms, with the precipitation gradient being more pronounced in CTL. In this region, CTL underestimates precipitation at most in-situ stations located at the bottom valley, and the bias can reach −2.0 mm or 75% less precipitation (Fig. 2d and e). Over the Mantaro Basin, CTL effectively captures the main precipitation patterns, particularly reflecting the higher values observed in the southern part of the basin compared to the central region (Fig. 2a-c). Biases in this basin are below 1 mm, which represent less than 25% compared to in-situ values. While in-situ data are scarce over the Andes-Amazon transition, CTL appears to perform well with lower bias over the highlands, although higher bias is observed below 1500 m a.s.l. (Fig. 2d and e). To further quantify the model's performance and

complement the spatial evaluation, the Root Mean Square Error (RMSE) between the simulated precipitation in the CTL experiment and the independent in-situ meteorological stations was calculated (provided in Supplementary Fig. S2). The spatial distribution of the RMSE reveals values generally ranging between 3 and 6 mm day^{-1} on the western slopes, while over the Mantaro basin and the eastern slopes, the errors are relatively higher, frequently exceeding 6 mm day^{-1}. While these RMSE values reflect the inherent challenges of simulating precise daily precipitation magnitudes at point locations over the highly complex Andean topography, the concurrent evaluation based on bias and spatial gradients (Fig. 2a-e) confirms that the CTL simulation captures the main regional precipitation features, rendering it a suitable baseline for our deforestation sensitivity experiments.

Fig. 2f-i shows the year-to-year variability obtained from daily precipitation data from in-situ measurements, PISCO, and CTL. These changes were evaluated by considering the four subregions in the study zone WSA, SMB, CMB, and AMA. Although only five wet periods are evaluated, Pearson correlation indicates that CTL represents the positive tendency in WSA and CMB, and the negative tendency in AMA. Furthermore, in the CMB and SMB regions, the minimum precipitation during the 2004–2005 period and the maximum during 2005–2006 are captured by CTL. This demonstrates the model's capability, similar to in-situ and PISCO data, to reflect the impacts of remote climatic conditions. For instance, the 2004–2005 (2005–2006) drought (strong rainfall) is linked to El Niño (La Niña) conditions (Fig. S1). CTL wind anomalies over the Andes (Fig. S3) also align with descriptions of westerly or easterly which facilitate the corresponding less or more moisture transport from the Amazon, respectively (Cai et al., 2020; Garreaud, 2009; among others). Also, the lower precipitation associated with negative anomalies of the Niño 1+2 over the western slope of the Andes, as suggested by Lavado-Casimiro and Espinoza (2014) and Lagos et al. (2008), during 2001–2002 period seems to be also reproduced by CTL over WSA. Additionally, the CTL mean exhibits a minimum during the first period (2001−2002), which coincides with the highest Tropical North Atlantic (TNA) warming observed across the five periods (Fig. S1). This TNA warming is associated with reduced moisture transport and drought conditions in the Peruvian Amazon (e.g., Espinoza et al., 2011; Lavado-Casimiro and Espinoza, 2014), a pattern that appears to extend its influence to the SMB, CMB, and WSA subregions.

3.2. Rainfall changes

As already mentioned, the DEF simulation results from modeling under the deforestation scenario, so hereafter, to show changes regarding control conditions (non-deforested, CTL), differences DEF-CTL are presented. For instance, Fig. 3a and b depict absolute and relative changes in precipitation, respectively. The spatial pattern exhibits a dipole-like distribution, where negative change is over the northeastern side and the positive one over the southwestern side, divided by an imaginary axis along the Mantaro Basin. The dipole-like pattern remains identifiable in the mean fields; however, statistical significance — calculated at the individual gridpoint level without spatial multiplicity correction — is largely confined to the negative pole, where it exhibits a dispersed spatial distribution, whereas the positive pole shows negligible significant areas. Over the Mantaro Basin, the majority of precipitation reduction is concentrated near the eastern border, particularly in the central and southern regions, with maximum decreases reaching up to 20% relative to CTL. Toward the easternmost areas, in the transition zone between the Andes and the Amazon, precipitation reductions are also evident. In this region, the most pronounced negative values can reach values above 3 mm day^{-1} with associated percentage that ranges from 10 up to 20% of CTL precipitation. We primarily observe a positive precipitation change along the higher elevations outside the western edge of the Mantaro Basin with more pronounced increases over ridge areas above 3500 m a.s.l. Increases can reach up to 1.0 mm day^{-1}, representing as much as a 20% rise in precipitation.

The dipole pattern is also clearly observed when analyzing precipitation changes as a function of elevation (Fig. S4). While the vertical profile shows an overall reduction between 500 and 3000 m a.s.l., this

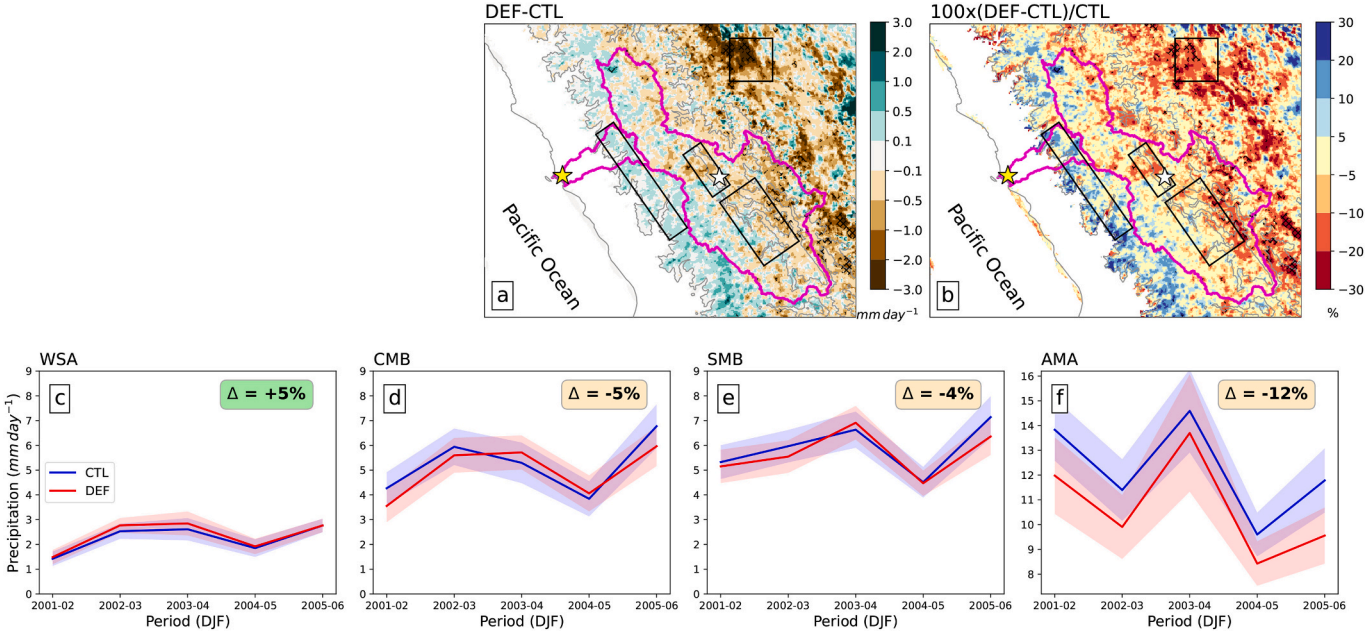

Fig. 3. (a) Difference in daily mean precipitation between DEF and CTL for all periods. (b) as in (a) but in percentage with respect to CTL, only when CTL is greater than 0.3 mm.day^{-1}. Yellow and white stars indicate Lima and Huancayo City, respectively. The Magenta line indicates the limits of the Mantaro and Rimac Basins. The gray contour line indicates 3500 m a.s.l. Black cross-hatching indicates statistically significant changes (p-value <0.10) calculated at the individual gridpoint level, without spatial multiplicity correction. (c), (d), (e), and (f) show year-to-year variability and error bars for CTL and DEF for subregions WSA, CMB, SMB and AMA, respectively. Values inside orange and green boxes indicate the relative average change (DEF-CTL) with respect to CTL. (For interpretation of the references to colour in this figure legend, the reader is referred to the web version of this article.)

signal is primarily driven by the stronger drying on the eastern slopes (consistent with the −12% reduction in AMA). A similar drying signal at these elevations was also simulated by Sierra et al. (2022) along the Zongo valley (perpendicular to the Andes) in Bolivia. In contrast, the western slope exhibits a distinct wetting signal centered around 4000 m a.s.l., confirming the positive anomalies found in the WSA subregion.

As previously mentioned, the CTL simulation exhibits year-to-year precipitation variability within the study subregions, aligning with climatic indices (Fig. 2f-i). The DEF simulation exhibits a similar temporal pattern (Fig. 3c-f), with maxima and minima occurring during the same periods; however, the magnitude and direction of the changes relative to CTL vary interannually. Consequently, the net change depends on the location of the subregion, consistent with the preceding spatial analysis. Specifically, in WSA there is an increase of 4% (+0.1 mm day^{-1}, Fig. 3c), whereas in CMB and SMB there are reductions of 5% (−0.3 mm day^{-1}, Fig. 3d) and 4% (−0.2 mm day^{-1}, Fig. 3e), respectively. Although none of these changes reach statistical significance, the reductions in CMB and SMB align with a physically coherent drying signal over most of the Mantaro Basin. In contrast, AMA experiences a significant 12% reduction (−1.4 mm day^{-1}), indicating a consistent precipitation deficit in DEF relative to CTL throughout the study period (Fig. 3f).

Fig. 4 shows the diurnal cycle according to normalized precipitation for CTL, DEF and the 2A25 product. CTL closely replicates the 2A25 product, particularly during peak precipitation hours, such as the afternoon in WSA, the late afternoon and early night in CMB and SMB, and the morning in AMA. While DEF generally follows the CTL diurnal cycle with minor deviations during peak hours (an increase in WSA and a decrease in CMB and SMB), AMA stands out with a pronounced reduction in precipitation intensity concentrated during its maximum precipitation period, between 00 LT and 10 LT. Quantitatively, the peak hourly rates (not shown) reach 0.33, 0.61, 0.35, and 1.11 mm hr^{-1} for WSA, CMB, SMB, and AMA, respectively. The changes in these peak rates are weak in most regions (−0.04 for CMB and SMB and + 0.02 mm hr^{-1} for WSA), consistent with the accumulated rainfall differences shown in Fig. 3, and no shifts in the timing of the peak hour were detected. Only in the AMA subregion is a more pronounced decrease observed (−0.18 mm hr^{-1}), which is also consistent with the spatial deficit presented for this region.

3.3. Circulation and moisture changes

Fig. 5 shows the vertical cross-section averaged between 10°S and 15°S concerning specific humidity and wind components in D01. Fig. 5a shows the average zonal-vertical wind and specific humidity. Over the Andes, we can observe easterly winds at upper levels (approximately at 200 hPa) associated with the Bolivian High. Similarly, east of the Andes, around 800 hPa, we can find an eastward wind component, linked to the LLJ that transports moisture from the tropics to the subtropics along the eastern Andean flank. Fig. 5b illustrates the DEF-CTL changes in the zonal-vertical wind and specific humidity. Consistent with Sierra et al. (2022), deforestation in D01 causes less injection of moisture from the surface into the atmosphere, inhibiting convection. This results in negative vertical wind changes over the Amazon, mainly between 800 and 200 hPa. Zonally, we found that a reduction in vertical velocity spans from the Amazon (55°W) to the Andean highlands (75°W) and vertically from 800 to 200 hPa, exhibiting locally statistically significant values over the Amazon and the Andes. Furthermore, notable negative changes are observed in the zonal wind above 800 hPa. This suggests a reinforcement of the easterlies above 600 hPa (the level of the Andean highlands) and a weakening of both the South American Monsoon and the LLJ. Regarding moisture, specific humidity exhibits a widespread decrease throughout the Amazonian atmosphere, extending even over the Andean range. However, locally statistically significant reductions are primarily confined to the lower troposphere (from the surface up to 800 hPa) over the Amazon Basin. This significant drying signal also prevails along the eastern slopes of the Andes, directly impacting the Amazon-Andes transition zone. Significant reductions in specific humidity are also observed in the upper troposphere of the Amazon and Andes, primarily above 300 hPa.

Contours in Fig. 5c display the CTL mean meridional wind, consistent with the typical austral summer circulation. It captures the Bolivian High at upper levels (positive/negative winds east/west of 63°W) and the characteristic monsoonal flow along the eastern Andes at mid-lower levels (negative values). Locally statistically significant positive changes are found over the deforested Amazon (around 55°W), indicating divergence as described by Sierra et al. (2022).

To observe the changes in the study area with more detail, Fig. 6a shows the integrated moisture fluxes and precipitable water between 1000 and 600 hPa. This layer approximates the atmospheric levels below the highest elevations of the Andes. The integrated moisture flux toward the southeast, associated with the LLJ, is clearly visible over the northeastern study region. Part of this flow is channeled through the Andes-Amazon transition zone valleys, carrying moisture to the Andean highlands. The vertically integrated moisture decreases (from 50 kg m^{-2}) with increasing altitude primarily due to a shallower atmosphere between the surface and the 600 hPa level. DEF-CTL shows a reduction in the intensity of moisture fluxes associated with the LLJ, resulting in less moisture transport to higher elevations, as demonstrated by the decrease in precipitable water along the valleys of the Andean-Amazon transition zone (Fig. 6b). For upper levels, Fig. 6c shows the integrated moisture fluxes and precipitable water over the mid-upper atmosphere (from 600 to 300 hPa). Consistent with Fig. 5a, easterly moisture fluxes in CTL can be observed and are associated with maximum precipitable water values of up to 10 kg m^{-2} over the eastern side of the Mantaro Basin. The CTL to DEF changes reveal a reduction in precipitable water, mainly to the east of the longitudinal line bisecting the Mantaro Basin

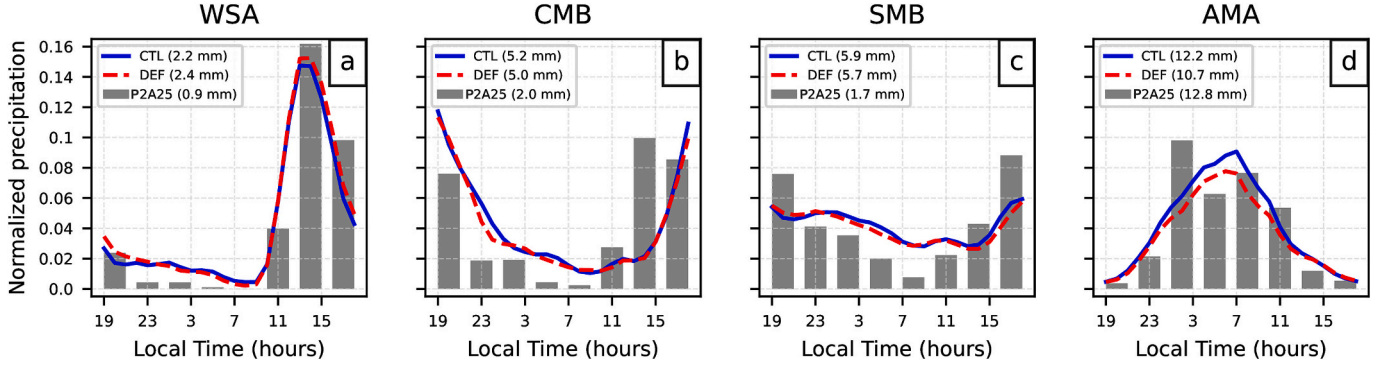

Fig. 4. Diurnal cycle of normalized precipitation for CTL, DEF, and P2A25 in subregions: (a) WSA, (b) CMB, (c) SMB, and (d) AMA. CTL and P2A25 use their own average daily precipitation as normalization factors. DEF uses the same factor as CTL to maintain relative differences. Daily average precipitation is annotated in the legend box.

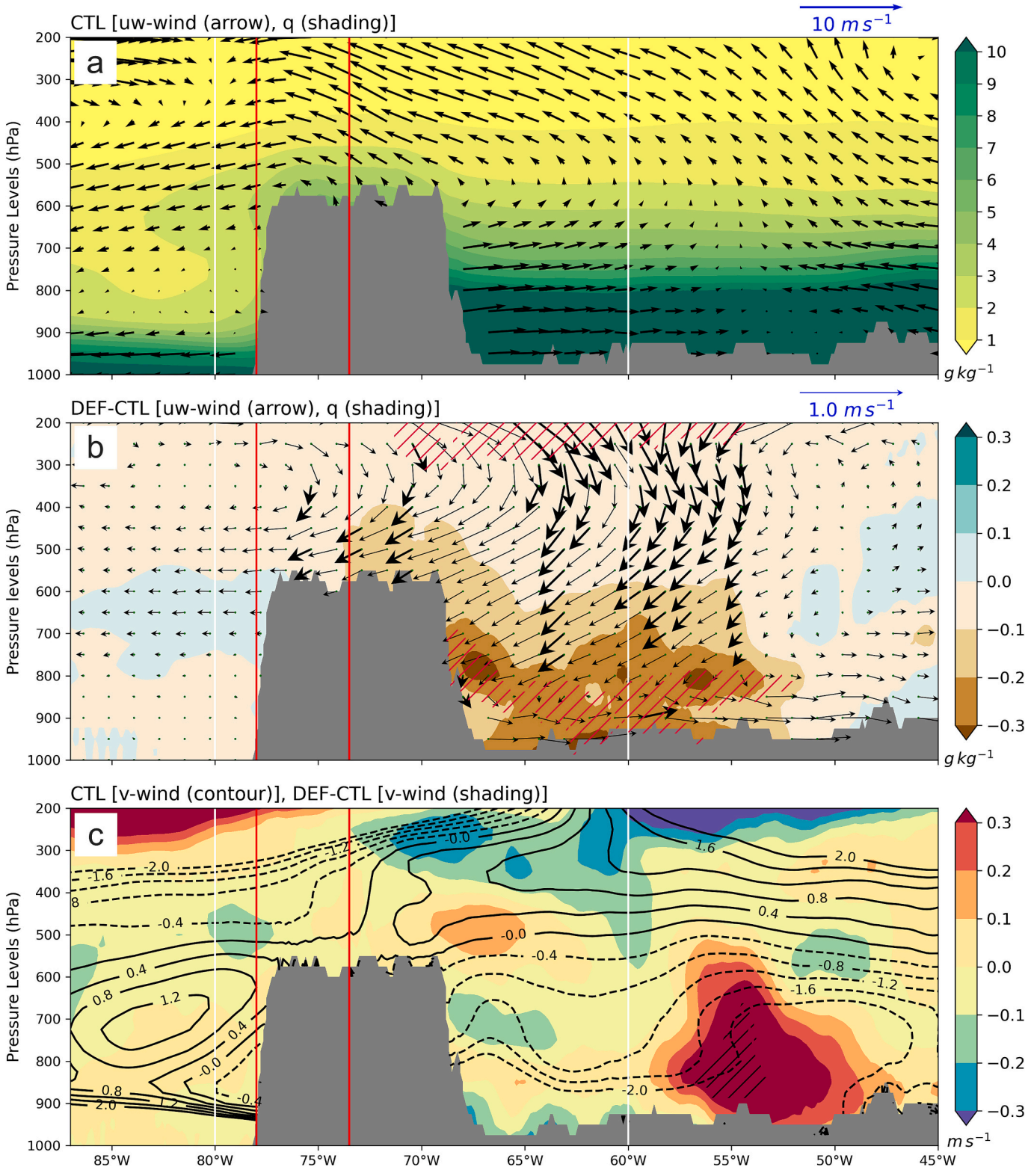

Fig. 5. Vertical cross-section averaged between 10°S and 15°S in domain D01. (a) Average zonal-vertical wind (vectors) and specific humidity (shading) for CTL. (b) Differences (DEF - CTL) in zonal-vertical wind and specific humidity. (c) Meridional wind for CTL (contours) and differences (DEF - CTL) (shading). Vertical white and red lines are included for reference to indicate the boundaries of domains D02 and D03, respectively. Statistical significance (p-value <0.10) is indicated by bold black arrows for winds, red hatching for specific humidity, and black hatching for meridional wind. Significance was calculated at the individual gridpoint level without spatial multiplicity correction. (For interpretation of the references to colour in this figure legend, the reader is referred to the web version of this article.)

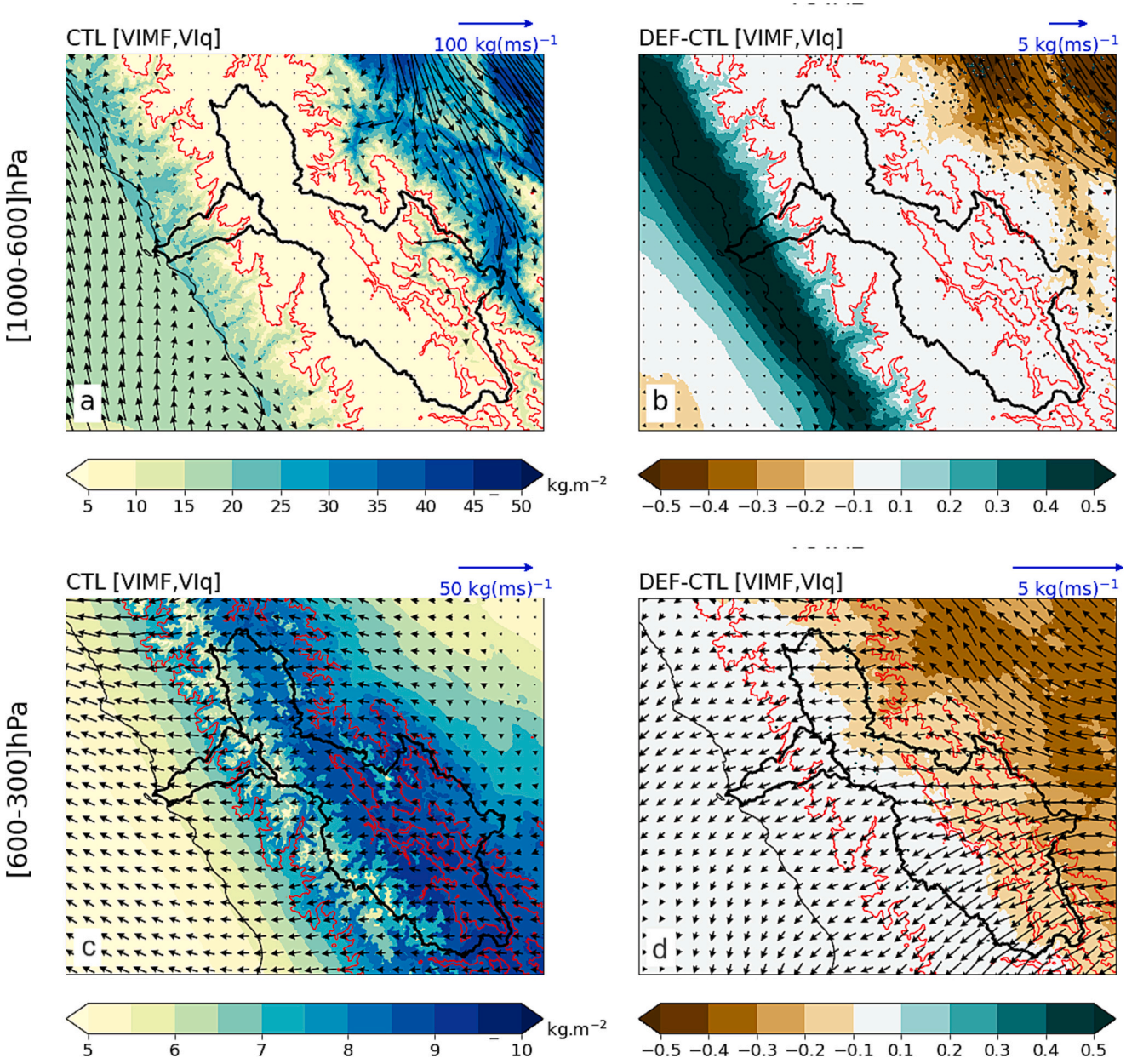

Fig. 6. (a) Vertically integrated moisture flux (VIMF) and precipitable water (VIq) between 1000 and 600 hPa. (b) Changes in VIMF and VIq for DEF relative to CTL considering the same level as in (a). (c) and (d) as in (a) and (b), but for the 600–300 hPa layer, respectively. The thick black line outlines the Mantaro and Rimac Basins, while the thin black line represents the coastline. The red line indicates the 3500 m a.s.l. contour. (For interpretation of the references to colour in this figure legend, the reader is referred to the web version of this article.)

(Fig. 6d). This spatial pattern is similar to the precipitation deficit presented in DEF relative to CTL (Fig. 3b). Fig. 6d also shows an increase in easterly moisture flux in mid-upper levels mainly associated with the increase of easterly winds rather than specific humidity, as the latter is reduced. (Fig. 5a-b).

Fig. 7 illustrates the diurnal cycle of the three wind components in a vertical profile for each subregion within the CTL simulation. Notably, the vertical wind component (Fig. 7a-d) in CTL exhibits updrafts during periods of peak precipitation (Fig. 4). Specifically, updrafts are most pronounced during 08–18 LT in WSA, 15–23 LT in CMB, 15–03 LT in SMB, and 23–11 LT in AMA. Comparing DEF to CTL (DEF–CTL), a locally statistically significant reduction in updraft intensity is observed in the AMA region. While a general weakening of vertical velocity spans from the near-surface up to the upper levels (~14 km) during the peak precipitation hours, statistically significant changes are more localized. Specifically, these anomalies are concentrated between 23 and 11 LT at altitudes ranging from 2 to 5 km. Additionally, some isolated statistically significant reductions are found at higher altitudes around 12 km. This pronounced signal coincides with the period of maximum convective activity and precipitation in the region. Similar to the AMA region, the CMB and SMB also show notable reductions in updraft intensity during peak precipitation hours (15–03 LT, Fig. 4). Conversely, the WSA exhibits a positive vertical velocity change across almost all atmospheric levels (locally statistically significant at upper levels), centered at 15 LT. This suggests a reinforcement of convection in this subregion.

Regarding the diurnal cycle of the zonal wind (Fig. 7e-h), the results are consistent with the daily averages shown in Fig. 5b, indicating a predominance of easterly winds. However, these figures reveal that this predominance is primarily observed above the mountain peaks (approximately above 5000 m a.s.l.). In all subregions, a negative

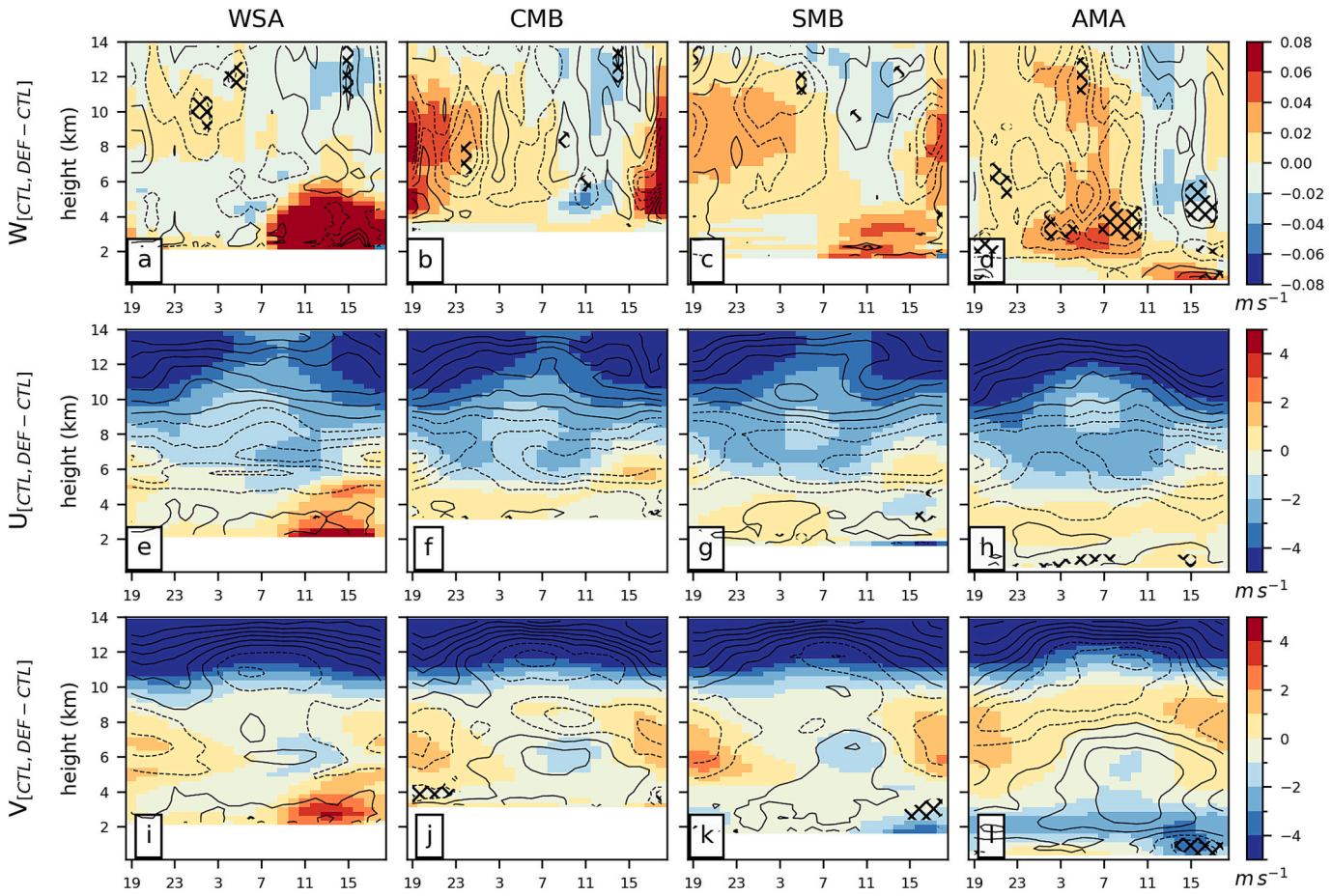

Fig. 7. Diurnal cycle of vertical wind component (W; shading) and the difference (DEF-CTL; contours) along the vertical profile for subregions: (a) WSA, (b) CMB, (c) SMB, and (d) AMA. Panels (e)-(h) and (i)-(l) are as in (a)-(d), but for zonal wind component U and meridional wind component V, respectively. Solid (dashed) contours represent positive or zero (negative) changes, with contour intervals of 0.2 cm s^{-1} for W and 0.1 m s^{-1} for U and V. Black cross-hatching indicates statistically significant changes (p-value <0.10) calculated at the individual gridpoint level, without spatial multiplicity correction.

change in the zonal wind in DEF compared to CTL is evident between 4000 and 10,000 m. This change persists throughout the day and appears to coincide—at least in WSA, CMB, and SMB—with the periods of maximum precipitation (Fig. 4). Furthermore, a weakening of the easterlies at upper levels is evident, consistent with the patterns in D01 (Fig. 5b). Finally, changes in the meridional wind at upper levels are positive (Fig. 7i-l), which is also consistent with the D01 domain. At lower levels, the most notable pattern of change occurs in the AMA region. Here, the observed anomaly is associated with a weakening of northerly winds between 07 and 11 LT, spanning from the surface up to 8000 m a.s.l., covering the altitudes where the LLJ is typically situated east of the Andes.

In the lower levels of WSA (Fig. 7e, i), the narrow valleys are oriented southwest-northeast. Thermally driven winds are prominent between 11 and 15 LT, characterized by positive U and V components as they ascend the slopes. The positive anomalies in both zonal and meridional winds (DEF–CTL) suggest a reinforcement of this local circulation phenomenon.

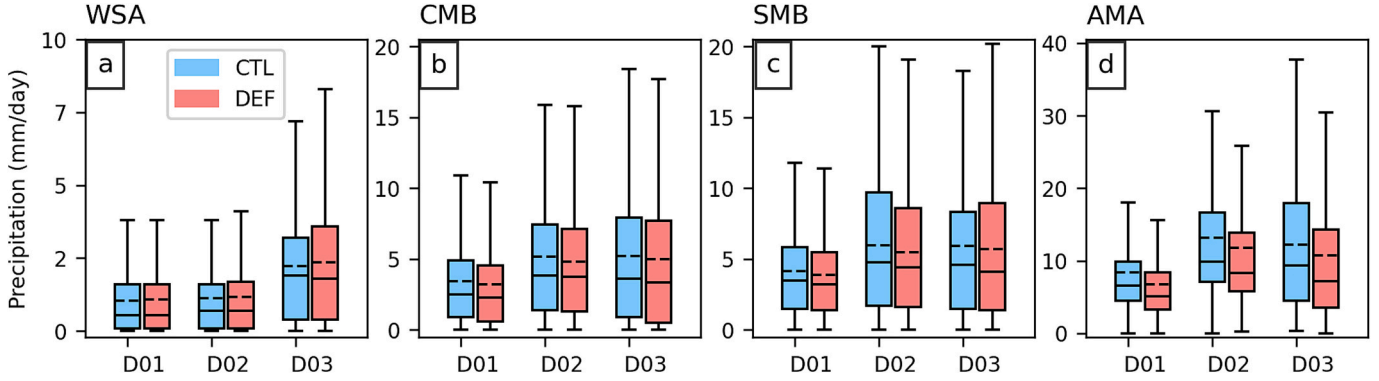

Fig. 8. Boxplots consider daily rainfall of CTL and DEF in subregions (a) WSA, (b) CMB, (c) SMB, and (d) AMA. Rainfall values are obtained from simulations in domains: D01 (15 km), D02 (5 km), and D03 (1 km). In addition to the median indicated with a line, the average of the distribution is depicted with a dashed line.

3.4. Precipitation response across scales

Fig. 8 shows boxplots of daily precipitation for CTL and DEF simulations across each subregion, as simulated in different spatial domains (D01, D02, and D03). As we had already found for the simulation covering our study region (D03), the DEF-CTL precipitation differences are negative in CMB, SMB, and AMA. While the observed differences reach local statistical significance across multiple grid points within the AMA subregion, the WSA exhibits a slight increase in precipitation that remains statistically non-significant. This behavior can be clearly observed in the boxplots labeled with "D03" on the x-axis of Fig. 8. The median precipitation values in DEF follow a similar behavior, characterized by a marked reduction in AMA. Similarly, results from the D01 and D02 domains reveal that these notable decreases in median and average precipitation are strictly confined to the AMA subregion.

Beyond DEF–CTL differences, some notable variations are present in the precipitation distribution across the spatial domains. For example, in the WSA, both the mean precipitation and the interquartile range (IQR) in D01 and D02 are 50% of that found in D03. In the other subregions (CMB, SMB, and AMA), D02 shows similar mean and median precipitation values, with less than 10% difference compared to D03. Regarding the IQR, the most significant changes occur in CMB and AMA, with reductions of 17% and 27% compared to those found in D03. We observe very notable changes when comparing CMB, SMB, and AMA subregions in D01 to D03: the medians and means are reduced by 20% to 35%, while the IQR decreases by 35% to 60%.

4. Discussion

4.1. Model representation of precipitation

We found that the model represents the spatial pattern well, based on in-situ data shown by previous works (Rau et al., 2017; Trachte et al., 2018; Saavedra et al., 2020), such as the increasing precipitation northeastward over the study region. We also encountered accompanying biases between −1 and + 1 mm. These bias values are also consistent with a previous work done by Saavedra et al. (2020), who compared them with simulations at a 3 km spatial resolution and encountered underestimation (overestimation) over the west slope of the Andes (Mantaro Basin). However, the impact on the western slope of the Andes is relatively stronger, as these bias values of less than 1 mm day^{-1} represent up to 25% overestimation in the Mantaro, but more than 75% underestimation over the western slope. However, the in-situ stations we used are mostly located in the lower part of these valleys' northeast-oriented (from the coast to higher elevations), where CTL seems to simulate very little precipitation, thus explaining these very negative biases. This underestimation can be deduced by comparing averages of all in-situ stations with all CTL grid points within WSA (Fig. 2f), rather than comparing independent in-situ stations with the corresponding nearest neighbor in CTL (Fig. 2e). Additionally, based on the diurnal cycle of vertical wind (Fig. 7a) and precipitation (Fig. 4a) and previous research (Trachte et al., 2018; Junquas et al., 2018, and Saavedra et al., 2020) we know that the majority of the precipitation events occur during the afternoon due to the effect of upslope flow, which tends to generate greater precipitation on the ridges than in the lower parts of the valleys. However, in the CTL simulation, this gradient tends to be overestimated with significantly underestimating rainfall in the lower parts. Other studies also suggest this type of overestimated precipitation gradient on slopes. Moya-Álvarez et al. (2025) demonstrate this using a 2 km spatial resolution model for two intense rainfall case studies in the Rimac Basin (part of WSA). Likewise, Mourre et al. (2016), using the Thompson microphysics scheme at 3 km resolution, reported strong precipitation gradients along its cross-section.

We acknowledge that our choice of the Purdue-Lin microphysics scheme is a source of uncertainty, as different schemes can alter convective timing and intensity (e.g., Thompson et al., 2004; Morrison et al., 2005). We selected the Purdue-Lin scheme based on an analysis of its performance in the parent simulations by Sierra et al. (2022). Their results showed that while biases can reach 50% in the slope of the Bolivian Andes, they decreased below 30% at higher elevations (above 3500 m), suggesting better performance for the high-Andean regions that are the focus of our study. However, this choice is also strongly supported by recent regional studies. A recent high-resolution (2 km) intercomparison by Llacza et al. (2025) for the nearby Peruvian Altiplano (Lake Titicaca basin) found that a configuration using Purdue-Lin (identical to ours) produced the lowest precipitation bias. Crucially, they noted that two configurations using the Thompson scheme and one using WSM6 microphysics tended to significantly overestimate precipitation, while a less sophisticated WSM3 scheme shows underestimation.

This context is critical, as our CTL simulation already shows a slight overestimation (up to 25%) in the Mantaro Basin (Fig. 2d). Extrapolating the findings of Llacza et al. (2025) suggests that using a scheme like Thompson would likely have exacerbated this positive bias. This is also consistent with Mourre et al. (2016), who used the Thompson scheme in a narrow northern Peruvian basin and found overestimation. Collectively, these studies suggest that our choice of Purdue-Lin was an appropriate selection to minimize known positive biases in the high Andes, and our findings of lower biases in the wide Mantaro valley are consistent with previous work (e.g., Saavedra et al., 2020).

Beyond the differences between CTL and DEF, a clear dependency of precipitation magnitude and variability on spatial resolution is evident (Fig. 8). This is primarily attributed to the model's ability to resolve convection-permitting processes and complex topography. In the WSA subregion, the daily precipitation intensity and its interquartile range (IQR) at 1 km (D03) are nearly double those found at 5 km or 15 km (Fig. 8a). This indicates that 1 km resolution is essential to resolve the narrow, northeast-oriented valleys where local thermal forcing drives rainfall. At coarser resolutions (D01 and D02), these topographic features are 'smoothed,' leading to weaker thermal forcing and a substantial underestimation of rainfall.

Conversely, in the Mantaro Basin (CMB and SMB) and the AMA transition, the transition from 5 km (D02) to 1 km (D03) shows minimal changes in mean values (<10%), suggesting that a 5 km resolution may be a sufficient 'threshold' to capture the main convective processes in these broader inter-Andean regions. However, a drastic reduction in both magnitude and daily variability is observed in the 15 km domain (D01) across all subregions, confirming that poorly resolved topography consistently dampens the precipitation signal by reducing the intensity of topographic triggering (e.g., El-Samra et al., 2017; Pontoppidan et al., 2017; Mourre et al., 2016).

4.2. Deforestation effects over the study zone

4.2.1. Mechanisms under Control Conditions

Before discussing the impacts of Amazon deforestation, it is crucial to establish that our Control simulation (CTL) correctly reproduces the physical mechanisms governing the region's hydroclimate. As documented in the literature, the regional circulation is characterized by moisture transport from the tropical Atlantic across the Amazon Basin, which is sustained by forest evapotranspiration and channeled southward (e.g., Marengo, 2006; Staal et al., 2018). The adequate representation of these processes in the D01 domain was validated by Sierra et al. (2022).

A key component of this circulation is the South American Low-Level Jet (LLJ), which develops east of the Andes. Fig. 5a and 7f clearly show this jet in the CTL run, with maximum intensity typically occurring around 850 hPa. As the LLJ moves southward, it redirects moisture-laden air toward the eastern slopes of the Andes (e.g., Espinoza et al., 2015; Junquas et al., 2018). In this region, the complex topography and deep valleys facilitate the upslope transport of moisture toward high-altitude areas like the Mantaro River Basin (Fig. 6a) (e.g., Chavez et al., 2020; Flores-Rojas et al., 2021; Llacza et al., 2025). Consequently,

intense precipitation is triggered at specific 'hot-spots' (such as the AMA subregion) where mechanical forcing by the Andean foothills lifts the moist air to deep convection, a process well represented in Fig. 7d (e.g. Kumar et al., 2019; Chavez and Takahashi, 2017; Espinoza et al., 2015). Furthermore, at levels above the mountain peaks (> 600 hPa), easterly winds provide an additional moisture source for the Andean highlands (e.g. Chavez et al., 2020; Garreaud, 1999), as evidenced by the mid-to-upper level flow in Fig. 7f and g. Finally, on the western slopes, precipitation is driven by afternoon thermal forcing along the northeast-oriented valleys (Fig. 7e and i). Here, the diurnal upslope circulation interacts with moist easterlies crossing the Andes (Fig. 6c and 7e) to reinforce local rainfall over the upper western slopes (Fig. 3b and 4a), in agreement with previous studies (e.g., Garreaud, 1999; Moya-Álvarez et al., 2025; Trachte et al., 2018).

Sierra et al. (2022) demonstrated over the coarse domain (D01) that Amazonian deforestation generates two key changes over the Amazon Basin: drier conditions or reduced specific humidity over the southwest and a reduction in the intensity of the LLJ. Our results suggest that these perturbed conditions propagate into the study zone (domain D03) via boundary forcing, directly altering the moisture availability and the low-level circulation that feeds the central Peruvian Andes.

4.2.2. *Response of the Eastern Slopes and the AMA Hot-spot*

The reduction in LLJ intensity identified by Sierra et al. (2022) and verified in this work, combined with the decrease in specific humidity (Fig. 6b and d), are the primary drivers of rainfall inhibition over the eastern region. The presence of westerly anomalies extending between 800 and 400 hPa (Fig. 5b and 7e-h) suggests that the dry conditions originating over the deforested Amazon propagate toward the Andean foothills, effectively suppressing updrafts and precipitation over the eastern slopes. Furthermore, the weakened LLJ leads to a reduction in mechanical updrafts, which in turn causes a more pronounced decrease

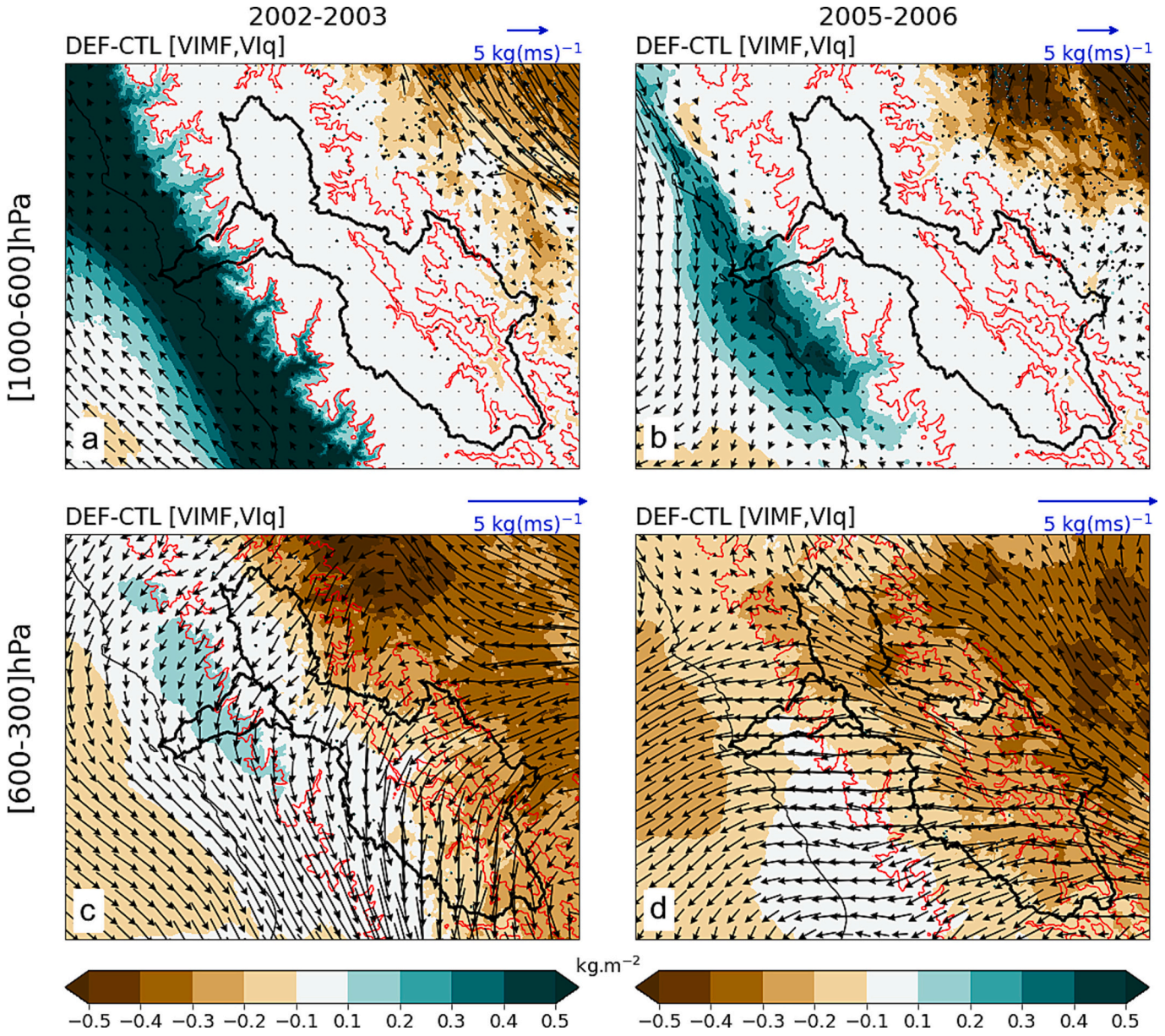

Fig. 9. Difference (DEF-CTL) of the vertically integrated moisture flux (VIMF) and precipitable water (VIq) between 1000 and 600 hPa for the period (a) 2002–2003 and (b) 2005–2006. (c) and (d) are as in (a) and (b), respectively, but for integration between 600 and 300 hPa. The thick black line outlines the Mantaro and Rimac Basins, while the thin black line represents the coastline. The red line indicates the 3500 m a.s.l. contour. (For interpretation of the references to colour in this figure legend, the reader is referred to the web version of this article.)

in rainfall within identified hot-spot zones (Fig. 3b and f). These inhibitory effects are most prominent during the hours of peak precipitation, specifically between 23 and 11 LT (Fig. 4d and 7d), where the total precipitation decreases by 1.5 mm, and vertical updraft velocities are significantly reduced by up to 0.06 m s^{-1} between 2 and 13 km altitude.

4.2.3. Moisture Transport toward the Andean Highlands (CMB and SMB)

Our findings suggest two distinct mechanisms that drive a physically coherent drying response over the highland Andes, including the Mantaro Basin. 1) Reduced Valley Channeling: A decrease in moisture flux is observed along the valleys connecting the Amazon to the highlands. This is associated with a reduction in LLJ intensity, with anomalous decelerations of the northerly wind averaging up to 0.2 m s^{-1} throughout the diurnal cycle (Fig. 4b-c, Fig. 6b and Fig. 7l). This weakened moisture transport through Andean passes is a known precursor for precipitation inhibition in the region, as described in previous studies on mountain-valley circulation (e.g., Falvey and Garreaud, 2005; Junquas et al., 2018) and high-altitude convective processes (e.g., Martínez-Castro et al., 2019; Flores-Rojas et al., 2021). 2) Mid-Upper Level Advection: In the deforestation scenario, an intensification of easterly winds at mid-to-upper levels (600–400 hPa) transports drier air from the Amazon directly over the Andes, bypassing the valley-scale interactions with the eastern slopes (Fig. 6d and Fig. 7f-h). These easterly winds anomalies increase by over 0.3 m s^{-1} precisely during the hours of peak precipitation, around 19 LT. While intensified easterlies are traditionally associated with increased moisture and rainfall in the highlands (e.g., Garreaud, 1999; Chavez et al., 2020), our results suggest that under deforestation, the advection of dry air from the basin becomes the dominant factor.

These two mechanisms exhibit inter-annual variability and do not necessarily occur during the same wet period. During 2002–2003, moisture reduction was more pronounced along the valleys between 1000 and 600 hPa (Fig. 9a) than at higher altitudes (Fig. 9c). In contrast, during 2005–2006, the drying was more notable at mid-to-upper levels between 600 and 300 hPa (Fig. 9d and b). This latter pattern extended this physically coherent drier condition across the Mantaro Basin and further westward.

4.2.4. Anomalous Precipitation increase on the Western Slopes (WSA)

In contrast to the general drying signal, a localized precipitation increase of up to 20% is observed over the ridges of the WSA. As established in previous studies (e.g. Moya-Álvarez et al., 2025; Trachte et al., 2018), diurnal upslope circulation and convective updrafts are the predominant mechanisms for rainfall in the upper western Andes. Our results suggest that Amazonian deforestation intensifies this phenomenon through a zonal dynamic response. Specifically, the deforestation-induced subsidence over the basin strengthens the easterly flow across the Andean barrier. This intensified cross-barrier flow, exhibiting anomalous westward increases of up to 0.3 m s^{-1} between 5 and 8 km altitude (Fig. 7e), reinforces the daytime anabatic circulation on the western slopes. This provides mechanical forcing for stronger upward motion during peak precipitation hours, typically around 14 LT (Fig. 4a and Fig. 7a). During these peak hours, this dynamical reinforcement is explicitly captured by anomalous positive zonal and meridional velocities (indicating upsloping winds; Fig. 7e and i) exceeding 0.1 m s^{-1}, alongside anomalous positive vertical velocities exceeding 0.06 m s^{-1} near the surface (between 2 and 4 km a.s.l.) (Fig. 7a). Consequently, this synchronized dynamical response is associated with a slight increase in peak hourly precipitation rates of 0.02 mm hr^{-1}. This mechanism is distinct from the LLJ-driven transport; here, the mechanical reinforcement of the intensified zonal flow is the dominant driver of rainfall enhancement, despite the overall drier conditions of the air masses.

Finally, a notable increase in precipitable water is observed between the shoreline and the western slopes of the Andes (Fig. 6b). When averaged across all periods, this increase can be attributed to a greater influx of moisture from the south under the DEF scenario. This phenomenon is particularly evident at levels between 700 and 600 hPa (Fig. S5). Specifically, the band of increased moisture shown in Fig. 6b is more pronounced during the 2002–2003 and 2004–2005 periods, coinciding with an intensification of southerly winds at these levels (not shown).

4.3. Study limitations

While this study provides a robust physical diagnostic of the hydrometeorological pathways between the Amazon and the Andes, certain feedback mechanisms remain simplified due to the model configuration. First, our simulations do not account for aerosol-cloud interactions. Biomass burning often accompanies deforestation, and the resulting aerosols could act as cloud condensation nuclei (CCN), potentially modifying cloud life cycles and precipitation efficiency beyond the purely dynamic changes reported here. For instance, Liu et al. (2020), using the coupled WRF-Chem model, found that biomass burning in the Amazon tends to reduce both rainfall rate and frequency. Consequently, the precipitation reduction identified in our study could be further exacerbated if aerosol effects were included, particularly considering that, in addition to the remote transport of Amazonian smoke (Bourgeois et al., 2015), there is a significant local contribution from crop residue burning within the agricultural areas of the Mantaro Basin (Estevan et al., 2019).

Second, the use of static land-cover (DEF scenario) does not capture dynamic vegetation feedbacks (e.g., forest dieback due to drought), which might further intensify the drying signal in a real-world context. Furthermore, our experimental design focuses on the Amazon Basin, neglecting potential deforestation within the study domain itself. Such local land-cover changes could induce an additional reduction in precipitation, particularly over the eastern slopes of the Andes, as demonstrated by Eghdami and Barros (2020).

Finally, while Purdue-Lin microphysics performed well for our high-Andean focus, further studies could test other microphysical schemes to help quantify the range of convective responses to deforestation-induced drying.

5. Conclusions

This study evaluated the impact of 40% Amazonian deforestation, consistent with a “business-as-usual” 2050 scenario, on precipitation patterns in the central Peruvian Andes. Using high-resolution (1 km) WRF simulations, we verified that the model accurately captures the regional diurnal cycle, despite an overestimation (up to 25%) in the Mantaro Basin in the central region of Peru and underestimation on the western slopes.

Our findings reveal a complex, dipole-like precipitation response to deforestation. On the eastern slopes and the Amazon-Andes transition (AMA), rainfall is inhibited (negative pole), particularly within identified precipitation hotspots where reductions can reach 10–20%. This inhibition is driven by a reduction in the intensity of the LLJ and a significant decrease in atmospheric moisture extending from the deforested Amazon. The weakened LLJ also diminishes moisture transport into the highlands through the deep valleys, such as the Mantaro Basin. These quantified precipitation changes represent a significant risk to regional water security, potentially impacting the Mantaro hydroelectric complex—which generates 19% of Peru's electricity—and threatening food security for the Lima metropolitan area (>10 millions of people).

In contrast, we identified a notable localized precipitation increase along the ridges of the western slopes (WSA, positive pole). This phenomenon is explained by a zonal dynamic response: deforestation-induced atmospheric subsidence over the Amazon Basin strengthens the easterly cross-barrier flow, reinforcing the daytime anabatic circulation. While this localized increase might offer a partial buffer, we acknowledge that the overall response of the Andean hydroclimate may be further modified by rising global CO_2 concentrations and land-cover

changes occurring within the Andean foothills themselves, which could interact with the Amazonian signal.

Based on our results, we propose the following actionable insights:

For Water-Resource Planners: The identified drier scenario — characterized by reduced precipitation and atmospheric moisture — in the Mantaro Basin and eastern slopes acts as a warning signal for future water availability. This suggests a risk of dry-season extension, necessitating contingency plans for prolonged deficits to safeguard water supply for human consumption and agricultural demands. Given the reliance of major population centers on these high-altitude catchments, adaptation strategies must prioritize potable water security alongside reservoir management.

For Policymakers: Our results physically demonstrate the teleconnection between Amazonian forest cover and Andean water security. This implies that conservation efforts in the Amazon are not merely a biodiversity issue but a critical component of the Andean economic stability. Effective adaptation requires trans-regional policies that treat the Amazon rainforest as effectively part of the hydrological infrastructure of the Andean nations.

For Earth-system Modelers: Our scale-dependency analysis establishes a guideline for regional climate downscaling: while a 5 km resolution is sufficient for representing the broad topography of inter-Andean basins like the Mantaro, convection-permitting scales (~1 km) are mandatory to correctly simulate the valley-ridge circulations (e.g., in the western slope of the Andes) and probably also necessary for convection in the Mantaro basin itself (Chavez et al., 2025). To reduce remaining uncertainties, we outline two priority next steps: (1) conducting coupled experiments that include aerosol-cloud interactions and dynamic vegetation to quantify potential feedback loops that could amplify the drying signal reported in this study; and (2) executing multi-year ensemble simulations to statistically separate the deforestation signal from interannual variability (e.g. ENSO; changes in the Atlantic SST).

Declaration of generative AI and AI-assisted technologies in the manuscript preparation process

During the preparation of this work the author(s) used Gemini and ChatGPT in order to improve the readability and language of the manuscript. After using this tool/service, the author(s) reviewed and edited the content as needed and take(s) full responsibility for the content of the published article.

CRediT authorship contribution statement

Miguel Saavedra: Writing – review & editing, Writing – original draft, Visualization, Validation, Software, Methodology, Investigation, Formal analysis, Data curation, Conceptualization. **Clementine Junquas:** Writing – review & editing, Supervision, Methodology, Formal analysis, Conceptualization. **Ken Takahashi:** Writing – review & editing, Methodology, Formal analysis, Conceptualization. **Yamina Silva:** Supervision, Project administration, Conceptualization. **Jhan-Carlo Espinoza:** Writing – review & editing, Conceptualization. **Juan-Pablo Sierra:** Writing – review & editing, Resources.

Declaration of competing interest

The authors declare that they have no known competing financial interests or personal relationships that could have appeared to influence the work reported in this paper.

Acknowledgements

Simulations were possible thanks to the "Laboratorio de Dinámica de Fluidos Geofísicos Computacional" at Instituto Geofísico del Perú (grants 101-2014-FONDECYT, SPIRALES2012 IRD-IGP, Manglares IGP-IDRC, PPR068 program). Additionally, some of the computations presented in this paper were performed using the GRICAD infrastructure (https://gricad.univ-grenoble-alpes.fr), which is partly supported by the Equip@Meso project (reference ANR-10-EQ.PX-29-01) of the programme Investissements d'Avenir supervised by the Agence Nationale pour la Recherche. Finally, we extend our gratitude to IRD-Peru for their institutional support. Special thanks are due to Claudia García for her valuable administrative assistance regarding the management of the first author's doctoral studies.

Appendix A. Supplementary data

Supplementary data to this article can be found online at https://doi.org/10.1016/j.atmosres.2026.109016.

Data availability

Data will be made available on request.

References

Asner, G.P., Martin, R.E., Tupayachi, R., Llactayo, W., 2017. Conservation assessment of the peruvian Andes and amazon based on mapped forest functional diversity. Biol. Conserv. 210, 80–88. https://doi.org/10.1016/j.biocon.2017.04.008.

Aybar, C., Fernández, C., Huerta, A., Lavado, W., Vega, F., Felipe-Obando, O., 2020. Construction of a high-resolution gridded rainfall dataset for Peru from 1981 to the present day. Hydrol. Sci. J. 65 (5), 770–785. https://doi.org/10.1080/02626667.2019.1649411.

Benton, G.S., Blackburn, R.T., Snead, V.O., 1950. The role of the atmosphere in the hydrologic cycle. Eos. Trans. AGU 31 (1), 61–73. https://doi.org/10.1029/tr031i001p00061.

Bourgeois, Q., Ekman, A.M.L., Krejci, R., 2015. Aerosol transport over the Andes from the amazon basin to the remote pacific ocean: A multiyear CALIOP assessment. J. Geophys. Res. Atmos. 120 (16), 8411–8425. https://doi.org/10.1002/2015jd023254.

Burde, G.I., Gandush, C., Bayarjargal, Y., 2006. Bulk recycling models with incomplete vertical mixing. Part II: Precipitation recycling in the amazon basin. J. Clim. 19 (8), 1473–1489. https://doi.org/10.1175/jcli3688.1.

Cai, W., McPhaden, M.J., Grimm, A.M., Rodrigues, R.R., Taschetto, A.S., Garreaud, R.D., et al., 2020. Climate impacts of the El Niño–southern oscillation on South America. Nat. Rev. Earth Environ. 1 (4), 215–231. https://doi.org/10.1038/s43017-020-0040-3.

Chavez, S.P., Takahashi, K., 2017. Orographic rainfall hot spots in the Andes-Amazon transition according to the TRMM precipitation radar and in situ data. J. Geophys. Res. Atmos. 122 (11), 5870–5882. https://doi.org/10.1002/2016JD026282.

Chavez, S.P., Silva, Y., Barros, A.P., 2020. High-Elevation monsoon precipitation processes in the Central Andes of Peru. J. Geophys. Res. Atmos. 125 (24). https://doi.org/10.1029/2020JD032947 e2020JD032947.

Chavez, S.P., Rojas, J.L.F., Takahashi, K., Silva, F.Y., 2025. Simulating stratiform precipitation with embedded convection in High-Elevation valleys using LES: the role of topographic detail. J. Geophys. Res. Atmos. 130 (23). https://doi.org/10.1029/2025jd043696.

Chen, S.H., Sun, W.Y., 2002. A one-dimensional time dependent cloud model. J. Meteorol. Soc. Japan. Ser. II 80 (1), 99–118. https://doi.org/10.2151/jmsj.80.99.

Costa, M.H., Foley, J.A., 2000. Combined effects of deforestation and doubled atmospheric CO2 concentrations on the climate of Amazonia. J. Clim. 13 (1), 18–34. https://doi.org/10.1175/1520-0442(2000)013.

Costa, M.H., Yanagi, S.N.M., Souza, P.J.O.P., Ribeiro, A., Rocha, E.J.P., 2007. Climate change in Amazonia caused by soybean cropland expansion, as compared to caused by pastureland expansion. Geophys. Res. Lett. 34 (7). https://doi.org/10.1029/2007GL029271.

Davidson, E.A., De Araújo, A.C., Artaxo, P., Balch, J.K., Brown, I.F., Bustamante, M.M.C., Coe, M.T., DeFries, R.S., Keller, M., Longo, M., Munger, J.W., Schroeder, W., Soares-Filho, B.S., Souza, C.M., Wofsy, S.C., 2012. The amazon basin in transition. Nature 481 (7381), 321–328. https://doi.org/10.1038/nature10717.

Debortoli, N.S., Dubreuil, V., Hirota, M., Filho, S.R., Lindoso, D.P., Nabucet, J., 2017. Detecting deforestation impacts in southern Amazonia rainfall using rain gauges. Int. J. Climatol. 37 (6). https://doi.org/10.1002/joc.4886.

Dirmeyer, P.A., Brubaker, K.L., DelSole, T., 2009. Import and export of atmospheric water vapor between nations. J. Hydrol. 365 (1–2), 11–22. https://doi.org/10.1016/j.jhydrol.2008.11.016.

Dudhia, J., 1989. Numerical study of convection observed during the winter monsoon experiment using a mesoscale two-dimensional model. J. Atmos. Sci. 46 (20). https://doi.org/10.1175/1520-0469(1989)046<3077:NSOCOD>2.0.CO;2.

Eghdami, M., Barros, A.P., 2020. Deforestation impacts on orographic precipitation in the tropical Andes. Front. Environ. Sci. 8. https://doi.org/10.3389/fenvs.2020.580159.

El-Samra, R., Bou-Zeid, E., El-Fadel, M., 2017. What model resolution is required in climatological downscaling over complex terrain? Atmos. Res. 203, 68–82. https://doi.org/10.1016/j.atmosres.2017.11.030.

Eltahir, E.A., Bras, R.L., 1994. Precipitation recycling in the amazon basin. Q. J. R. Meteorol. Soc. 120 (518), 861–880. https://doi.org/10.1002/qj.49712051806.
Espinoza Villar, J.C., Ronchail, J., Guyot, J.L., Cochonneau, G., Naziano, F., Lavado, W., De Oliveira, E., Pombosa, R., Vauchel, P., 2009. Spatio-temporal rainfall variability in the amazon basin countries (Brazil, Peru, Bolivia, Colombia, and Ecuador). Int. J. Climatol. 29, 1574–1594. https://doi.org/10.1002/joc.1791.
Espinoza, J.C., Ronchail, J., Guyot, J.L., Junquas, C., Vauchel, P., Lavado, W., Drapeau, G., Pombosa, R., 2011. Climate variability and extreme drought in the upper Solimões river (western amazon basin): Understanding the exceptional 2010 drought. Geophys. Res. Lett. 38 (13), n/a. https://doi.org/10.1029/2011gl047862.
Espinoza, J.C., Chavez, S., Ronchail, J., Junquas, C., Takahashi, K., Lavado, W., 2015. Rainfall hotspots over the southern tropical Andes: Spatial distribution, rainfall intensity, and relations with large-scale atmospheric circulation. Water Resour. Res. 51 (5), 3459–3475. https://doi.org/10.1002/2014wr016273.
Espinoza, J.C., Garreaud, R., Poveda, G., Arias, P.A., Molina-Carpio, J., Masiokas, M., Viale, M., Scaff, L., 2020. Hydroclimate of the Andes part I: main climatic features. Front. Earth Sci. 8. https://doi.org/10.3389/feart.2020.00064.
Espinoza, J.C., Arias, P.A., Moron, V., Junquas, C., Segura, H., Sierra-Pérez, J.P., Wongchuig, S., Condom, T., 2021. Recent changes in the atmospheric circulation patterns during the dry-to-wet transition season in south tropical South America (1979–2020): impacts on precipitation and fire season. J. Clim. 34 (22). https://doi.org/10.1175/JCLI-D-21-0303.1.
Espinoza, J., Jimenez, J.C., Marengo, J.A., Schongart, J., Ronchail, J., Lavado-Casimiro, W., Ribeiro, J.V.M., 2024. The new record of drought and warmth in the Amazon in 2023 related to regional and global climatic features. Sci. Rep. 14 (1). https://doi.org/10.1038/s41598-024-58782-5.
Estevan, R., Martínez-Castro, D., Suarez-Salas, L., Moya, A., Silva, Y., 2019. First two and a half years of aerosol measurements with an AERONET sunphotometer at the Huancayo observatory, Peru. Atmos. Environ. X 3, 100037. https://doi.org/10.1016/j.aeaoa.2019.100037.
Eva, H.D., Belward, A.S., De Miranda, E.E., Di Bella, C.M., Gond, V., Huber, O., Jones, S., Sgrenzaroli, M., Fritz, S., 2004. A land cover map of South America. Glob. Chang. Biol. 10 (5), 731–744. https://doi.org/10.1111/j.1529-8817.2003.00774.x.
Falvey, M., Garreaud, R.D., 2005. Moisture variability over the south american altiplano during the South American low level jet experiment (SALLJEX) observing season. J. Geophys. Res. Atmos. 110 (D22). https://doi.org/10.1029/2005jd006152.
Flores-Rojas, J.L., Moya-Álvarez, A.S., Valdivia-Prado, J.M., Piñas-Laura, M., Kumar, S., Karam, H.A., Villalobos-Puma, E., Martínez-Castro, D., Silva, Y., 2021. On the dynamic mechanisms of intense rainfall events in the Central Andes of Peru, Mantaro valley. Atmos. Res. 248, 105188. https://doi.org/10.1016/j.atmosres.2020.105188.
Fu, R., Yin, L., Li, W., Arias, P.A., Dickinson, R.E., Huang, L., Chakraborty, S., Fernandes, K., Liebmann, B., Fisher, R., Myneni, R.B., 2013. Increased dry-season length over southern Amazonia in recent decades and its implication for future climate projection. Proc. Natl. Acad. Sci. USA 110 (45). https://doi.org/10.1073/pnas.1302584110.
Funk, C., Peterson, P., Landsfeld, M., Pedreros, D., Verdin, J., Shukla, S., et al., 2015. The climate hazards infrared precipitation with stations—a new environmental record for monitoring extremes. Sci. Data 2 (1), 1–21, 150066. https://doi.org/10.1038/sdata.2015.66.
Garreaud, R., 1999. Multiscale analysis of the summertime precipitation over the Central Andes. Mon. Weather Rev. 127 (5), 901–921. https://doi.org/10.1175/1520-0493(1999)127.
Garreaud, R.D., 2009. The Andes climate and weather. Adv. Geosci. 22, 3. https://doi.org/10.5194/adgeo-22-3-2009.
Giráldez, L., Silva, Y., Zubieta, R., Sulca, J., 2020. Change of the rainfall seasonality over central Peruvian Andes: Onset, end, duration and its relationship with large-scale atmospheric circulation. Climate 8 (2). https://doi.org/10.3390/cli8020023.
Grell, G.A., Dévényi, D., 2002. A generalized approach to parameterizing convection combining ensemble and data assimilation techniques. Geophys. Res. Lett. 29 (14). https://doi.org/10.1029/2002gl015311.
Hersbach, H., Bell, B., Berrisford, P., Hirahara, S., Horányi, A., Muñoz-Sabater, J., Nicolas, J., Peubey, C., Radu, R., Schepers, D., Simmons, A., Soci, C., Abdalla, S., Abellan, X., Balsamo, G., Bechtold, P., Biavati, G., Bidlot, J., Bonavita, M., et al., 2020. The ERA5 global reanalysis. Q. J. R. Meteorol. Soc. 146 (730). https://doi.org/10.1002/qj.3803.
Hirota, M., Holmgren, M., van Nes, E.H., Scheffer, M., 2011. Global resilience of tropical forest and savanna to critical transitions. Science 334 (6053). https://doi.org/10.1126/science.1210657.
Hong, S.Y., Noh, Y., Dudhia, J., 2006. A new vertical diffusion package with an explicit treatment of entrainment processes. Mon. Weather Rev. 134 (9). https://doi.org/10.1175/MWR3199.1.
INEI, 2021a. Compendio estadístico Perú 2021, parte 1, Biblioteca Nacional del Perú, 2021–13020. https://cdn.www.gob.pe/uploads/document/file/3117981/Compendio%20Estad%C3%ADstico.%20Per%C3%BA%202021%20%28Tomo%201%29.pdf?v=1653079933.
INEI, 2021b. Compendio estadístico Perú 2021, parte 2. Biblioteca Nacional del Perú, 2021–13022. https://cdn.www.gob.pe/uploads/document/file/3117982/Compendio%20Estad%C3%ADstico.%20Per%C3%BA%202021%20%28Tomo%202%29.pdf?v=1653079933.
Instituto Geofísico del Perú, 2005. Diagnóstico de la Cuenca del Mantaro bajo la visión del cambio climático. CONAM, Lima, Perú, p. 107. Available online at http://hdl.handle.net/20.500.12816/715.
Junquas, C., Takahashi, K., Condom, T., Espinoza, J.-C., Chavez, S., Sicart, J.-E., Lebel, T., 2018. Understanding the influence of orography on the precipitation diurnal cycle and the associated atmospheric processes in the Central Andes. Clim. Dyn. 0 (0), 0. https://doi.org/10.1007/s00382-017-3858-8.
Junquas, C., Heredia, M.B., Condom, T., Ruiz-Hernández, J.C., Campozano, L., Dudhia, J., Espinoza, J.C., Menegoz, M., Rabatel, A., Sicart, J.E., 2022. Regional climate modeling of the diurnal cycle of precipitation and associated atmospheric circulation patterns over an Andean glacier region (Antisana, Ecuador). Clim. Dyn. 58 (11–12), 3075–3104. https://doi.org/10.1007/s00382-021-06079-y.
Klein, C., Hänchen, L., Potter, E.R., Junquas, C., Harris, B.L., Maussion, F., 2023. Untangling the importance of dynamic and thermodynamic drivers for wet and dry spells across the tropical Andes. Environ. Res. Lett. 18 (3), 034002. https://doi.org/10.1088/1748-9326/acb72b.
Kumar, S., Vidal, Y.S., Moya-Álvarez, A.S., Martínez-Castro, D., 2019. Effect of the surface wind flow and topography on precipitating cloud systems over the Andes and associated amazon basin: GPM observations. Atmos. Res. 225, 193–208.
Lagos, P., Silva, Y., Nickl, E., Mosquera, K., 2008. El Niño - related precipitation variability in Peru. Adv. Geosci. 14, 231–237. https://doi.org/10.5194/adgeo-14-231-2008.
Lavado Casimiro, W.S., Labat, D., Ronchail, J., Espinoza, J.C., Guyot, J.L., 2013. Trends in rainfall and temperature in the Peruvian Amazon-Andes basin over the last 40years (1965-2007). Hydrol. Process. 27 (20), 2944–2957. https://doi.org/10.1002/hyp.9418.
Lavado-Casimiro, W., Espinoza, J.C., 2014. Impactos de El Niño y La Niña en las lluvias del Perú (1965-2007). Revista Brasileira de Meteorologia 29, 171–182.
Leite-Filho, A.T., Soares-Filho, B.S., Davis, J.L., Abrahão, G.M., Börner, J., 2021. Deforestation reduces rainfall and agricultural revenues in the brazilian amazon. Nat. Commun. 12 (1). https://doi.org/10.1038/s41467-021-22840-7.
Liu, L., Cheng, Y., Wang, S., Wei, C., Pöhlker, M.L., Pöhlker, C., Artaxo, P., Shrivastava, M., Andreae, M.O., Pöschl, U., Su, H., 2020. Impact of biomass burning aerosols on radiation, clouds, and precipitation over the amazon: Relative importance of aerosol–cloud and aerosol–radiation interactions. Atmos. Chem. Phys. 20 (21), 13283–13301. https://doi.org/10.5194/acp-20-13283-2020.
Llacza, A., Paredes, J., Llamocca, J., Saavedra, M., Fita, L., Ruiz, C., Junquas, C., 2025. Improved spatial representation of precipitation and air surface temperature over highlands of the southern tropical Andes (Lake Titicaca region) during an austral summer using the WRF model. Atmos. Res. 325, 108262. https://doi.org/10.1016/j.atmosres.2025.108262.
Malhi, Y., Roberts, J.T., Betts, R.A., Killeen, T.J., Li, W., Nobre, C.A., 2008. Climate change, deforestation, and the fate of the Amazon. Science 319 (5860). https://doi.org/10.1126/science.1146961.
Marengo, J.A., 2006. On the hydrological cycle of the amazon basin: A historical review and current state-of-the-art. Revista brasileira de meteorologia 21 (3), 1–19.
Martínez-Castro, D., Kumar, S., Flores Rojas, J.L., Moya-Álvarez, A., Valdivia-Prado, J. M., Villalobos-Puma, E., Del Castillo-Velarde, C., Silva-Vidal, Y., 2019. The impact of microphysics parameterization in the simulation of two convective rainfall events over the Central Andes of Peru using WRF-ARW. Atmosphere 10 (8), 442. https://doi.org/10.3390/atmos10080442.
MINAM, 2012. Inventario y Evaluación del Patrimonio Natural en los Ecosistemas de Selva Alta del Parque Nacional Yanachaga Chemillén. Ministerio del Ambiente. Retrieved from. https://cdn.www.gob.pe/uploads/document/file/11907/Inventario-de-Ecosistemas-de-Selva-Alta-Yanachaga.pdf?v=1530547990.
Mittermeier, R.A., Turner, W.R., Larsen, F.W., Brooks, T.M., Gascon, C., 2011. Global biodiversity conservation: the critical role of hotspots. In: Springer eBooks, pp. 3–22. https://doi.org/10.1007/978-3-642-20992-5_1.
Mlawer, E.J., Taubman, S.J., Brown, P.D., Iacono, M.J., Clough, S.A., 1997. Radiative transfer for inhomogeneous atmospheres: RRTM, a validated correlated-k model for the longwave. J. Geophys. Res. Atmos. 102 (D14), 16663–16682.
Morrison, H., Curry, J.A., Khvorostyanov, V.I., 2005. A new Double-Moment microphysics parameterization for application in cloud and climate models. Part I: description. J. Atmos. Sci. 62 (6), 1665–1677. https://doi.org/10.1175/jas3446.1.
Mourre, L., Condom, T., Junquas, C., Lebel, T., Sicart, J., Figueroa, R., Cochachin, A., 2016. Spatio-temporal assessment of WRF, TRMM and in situ precipitation data in a tropical mountain environment (Cordillera Blanca, Peru). Hydrol. Earth Syst. Sci. 20 (1), 125–141. https://doi.org/10.5194/hess-20-125-2016.
Moya-Alvarez, A.S., Martínez-Castro, D., Flores, J.L., Silva, Y., 2018. Sensitivity study on the influence of parameterization schemes in WRF_ARW model on short-and medium-range precipitation forecasts in the Central Andes of Peru. Adv. Meteorol. 2018. https://doi.org/10.1155/2018/1381092.
Moya-Álvarez, A.S., Silva, Y., Villalobos-Puma, E., Saavedra-Huanca, M., Del Castillo, C., Kumar, S., Valdivia-Prado, J.M., 2025. Extreme precipitation events associated with summer rains in the western slope of the Peruvian Andes using a numerical modeling and weather radar data: Case studies. Pure Appl. Geophys. https://doi.org/10.1007/s00024-025-03834-8.
Nobre, C.A., Borma, L.D.S., 2009. "Tipping points" for the Amazon forest. Curr. Opin. Environ. Sustain. 1 (1). https://doi.org/10.1016/j.cosust.2009.07.003.
Nobre, C.A., Sampaio, G., Borma, L.S., Castilla-Rubio, J.C., Silva, J.S., Cardoso, M., 2016. Land-use and climate change risks in the amazon and the need of a novel sustainable development paradigm. Proc. Natl. Acad. Sci. USA 113 (39), 10759–10768. https://doi.org/10.1073/pnas.1605516113.
Paulson, C.A., 1970. The mathematical representation of wind speed and temperature profiles in the unstable atmospheric surface layer. J. Appl. Meteorol. 9 (6). https://doi.org/10.1175/1520-0450(1970)009<0857:tmrows>2.0.co;2.
Pontoppidan, M., Reuder, J., Mayer, S., Kolstad, E.W., 2017. Downscaling an intense precipitation event in complex terrain: the importance of high grid resolution. Tellus A: Dyn. Meteorol. Oceanogr. 69 (1), 1271561. https://doi.org/10.1080/16000870.2016.1271561.
Rau, P., Bourrel, L., Labat, D., Melo, P., Dewitte, B., Frappart, F., Lavado, W., Felipe, O., 2017. Regionalization of rainfall over the Peruvian pacific slope and coast. Int. J. Climatol. 37 (1), 143–158. https://doi.org/10.1002/joc.4693.

Reynolds, R.W., Rayner, N.A., Smith, T.M., Stokes, D.C., Wang, W., 2002. An improved in situ and satellite SST analysis for climate. J. Clim. 15, 1609–1625. https://doi.org/10.1175/1520-0442(2002)015<1609:AIISAS>2.0.CO;2.

Rosales, A.G., Junquas, C., da Rocha, R.P., Condom, T., Espinoza, J.-C., 2022. Valley–mountain circulation associated with the diurnal cycle of precipitation in the Tropical Andes (Santa River Basin, Peru). Atmosphere 13 (2), 344. https://doi.org/10.3390/atmos13020344.

Saavedra, M., Takahashi, K., 2017. Physical controls on frost events in the Central Andes of Peru using in situ observations and energy flux models. Agric. For. Meteorol. 239, 58–70. https://doi.org/10.1016/j.agrformet.2017.02.019.

Saavedra, M., Junquas, C., Espinoza, J.-C., Silva, Y., 2020. Impacts of topography and land use changes on the air surface temperature and precipitation over the central Peruvian Andes. Atmos. Res. 234 (2014), 104711. https://doi.org/10.1016/J.ATMOSRES.2019.104711.

Sampaio, G., Nobre, C., Costa, M.H., Satyamurty, P., Soares-Filho, B.S., Cardoso, M., 2007. Regional climate change over eastern Amazonia caused by pasture and soybean cropland expansion. Geophys. Res. Lett. 34 (17). https://doi.org/10.1029/2007GL030612.

Segura, H., Junquas, C., Espinoza, J.C., Vuille, M., Jauregui, Y.R., Rabatel, A., Condom, T., Lebel, T., 2019. New insights into the rainfall variability in the tropical Andes on seasonal and interannual time scales. Clim. Dyn. 0 (0), 0. https://doi.org/10.1007/s00382-018-4590-8.

Segura, H., Espinoza, J.C., Junquas, C., Lebel, T., Vuille, M., Garreaud, R., 2020. Recent changes in the precipitation-driving processes over the southern tropical Andes/western amazon. Clim. Dyn. 54 (5–6), 2613–2631. https://doi.org/10.1007/s00382-020-05132-6.

Sierra, J.P., Junquas, C., Espinoza, J.C., Segura, H., Condom, T., Andrade, M., Molina-Carpio, J., Ticona, L., Mardoñez, V., Blacutt, L., Polcher, J., Rabatel, A., Sicart, J.E., 2022. Deforestation impacts on Amazon-Andes hydroclimatic connectivity. Clim. Dyn. 58 (9–10), 2609–2636. https://doi.org/10.1007/s00382-021-06025-y.

Silva Junior, C.H.L., Pessôa, A.C.M., Carvalho, N.S., Reis, J.B.C., Anderson, L.O., Aragão, L.E.O.C., 2021. The Brazilian Amazon deforestation rate in 2020 is the greatest of the decade. Nat. Ecol. Evol. 5 (2). https://doi.org/10.1038/s41559-020-01368-x.

Skamarock, W.C., Klemp, J.B., Dudhia, J., Gill, D.O., Liu, Z., Berner, J., et al., 2019. A Description of the Advanced Research WRF Model Version 4.1 (No. NCAR/TN-556+STR). https://doi.org/10.5065/1dfh-6p97.

Soares-Filho, B.S., Nepstad, D.C., Curran, L.M., Cerqueira, G.C., Garcia, R.A., Ramos, C. A., Voll, E., McDonald, A., Lefebvre, P., Schlesinger, P., 2006. Modelling conservation in the amazon basin. Nature 440 (7083), 520–523. https://doi.org/10.1038/nature04389.

Staal, A., Tuinenburg, O.A., Bosmans, J.H.C., Holmgren, M., Van Nes, E.H., Scheffer, M., Zemp, D.C., Dekker, S.C., 2018. Forest-rainfall cascades buffer against drought across the amazon. Nat. Clim. Chang. 8 (6), 539–543. https://doi.org/10.1038/s41558-018-0177-y.

Sulca, J., Vuille, M., Silva, Y., Takahashi, K., 2016. Teleconnections between the Peruvian Central Andes and Northeast Brazil during extreme rainfall events in austral summer. J. Hydrometeorol. 17 (2), 499–515. https://doi.org/10.1175/jhm-d-15-0034.1s.

Swann, A.L.S., Longo, M., Knox, R.G., Lee, E., Moorcroft, P.R., 2015. Future deforestation in the Amazon and consequences for South American climate. Agric. For. Meteorol. 214–215. https://doi.org/10.1016/j.agrformet.2015.07.006.

Thompson, G., Rasmussen, R.M., Manning, K., 2004. Explicit forecasts of winter precipitation using an improved bulk microphysics scheme. Part i: description and sensitivity analysis. Mon. Weather Rev. 132 (2), 519–542. https://doi.org/10.1175/1520-0493(2004)132.

Trachte, K., Seidel, J., Figueroa, R., Otto, M., Bendix, J., 2018. Cross-Scale precipitation variability in a semiarid catchment area on the western slopes of the Central Andes. J. Appl. Meteorol. Climatol. 57 (3), 675–694. https://doi.org/10.1175/JAMC-D-17-0207.1.

Wilks, D.S., 2019. Statistical Methods in the Atmospheric Sciences, fourth ed. Elsevier, Amsterdam.

Wongchuig, S., Espinoza, J.C., Condom, T., Segura, H., Ronchail, J., Arias, P.A., Junquas, C., Rabatel, A., Lebel, T., 2022. A regional view of the linkages between hydro-climatic changes and deforestation in the southern amazon. Int. J. Climatol. 42 (7). https://doi.org/10.1002/joc.7443.